Accepted for publication in the Astrophysical Journal Supplement,
the COUP Special Issue

# *Chandra* Orion Ultradeep Project: Observations and Source Lists

K. V. Getman[1], E. Flaccomio[2], P. S. Broos[1], N. Grosso[3], M. Tsujimoto[1], L. Townsley[1], G. P. Garmire[1], J. Kastner[4], J. Li[4], F. R. Harnden, Jr.[5], S. Wolk[5], S. S. Murray[5], C. J. Lada[5], A. A. Muench[5], M. J. McCaughrean[6], G. Meeus[6], F. Damiani[2], G. Micela[2], S. Sciortino[2], J. Bally[7], L. A. Hillenbrand[8], W. Herbst[9], T. Preibisch[10], E. D. Feigelson[1]

## ABSTRACT

We present a description of the data reduction methods and the derived catalog of more than 1600 X-ray point sources from the exceptionally deep January 2003 Chandra X-ray Observatory (*Chandra*) observation of the Orion Nebula Cluster and embedded populations around OMC-1. The observation was obtained with *Chandra*'s Advanced CCD Imaging Spectrometer (ACIS) and has been nicknamed the *Chandra* Orion Ultradeep Project (COUP). With an 838 ks exposure made over a continuous period of 13.2 days, the COUP observation provides the most uniform and comprehensive dataset on the X-ray emission of normal stars ever obtained in the history of X-ray astronomy.

*Subject headings:* ISM: individual (Orion Nebula, OMC-1) − open clusters and associations: individual (Orion) − stars: early-type − stars: pre-main-sequence − X-Rays: stars

---

[1]Department of Astronomy & Astrophysics, Pennsylvania State University, 525 Davey Laboratory, University Park, PA 16802

[2]INAF, Osservatorio Astronomico di Palermo G. S. Vaiana, Piazza del Parlamento 1, I-90134 Palermo, Italy

[3]Laboratoire d'Astrophysique de Grenoble, Universite Joseph Fourier, BP 53, 38041 Grenoble Cedex 9, France

[4]Chester F. Carlson Center for Imaging Science, Rochester Institute of Technology, 54 Lomb Memorial Drive, Rochester, NY 14623

[5]Smithsonian Astrophysical Observatory, 60 Garden Street, Cambridge, MA 02138

[6]Astrophysikalisches Institut Potsdam, An der Sternwarte 16, D-14482 Potsdam, Germany

[7]Center for Astrophysics and Space Astronomy, University of Colorado at Boulder, CB 389, Boulder, CO 80309

[8]Department of Astronomy, California Institute of Technology, Pasadena, CA 91125

[9]Max-Planck-Institut fur Astronomie, Konigstuhl 17, 69117 Heidelberg, Germany

[10]Max-Planck-Institut fur Radioastronomie, Auf dem Hugel 69, 53121 Bonn, Germany

## 1. Introduction

The processes of star formation and early stellar evolution have proved to be complex in many respects. Gravitational collapse can be hindered by magnetic and turbulent pressures and is accompanied by collimated jets and outflows during the protostellar phase. The dynamics and evolution of circumstellar disks where planets form are still under study. The birth of stars rarely occurs in isolation. Most stars form in a hierarchy ranging from binaries to rich clusters. These processes, which take place in thermodynamically cold and neutral media with characteristic energies of $\ll 1$ eV per particle, paradoxically produce and are subject to violent high energy processes with characteristic energies of $\gtrsim 10^3$ eV. The principal evidence for this is X-ray emission (and sometimes nonthermal radio emission) from stars throughout their pre-main sequence (PMS) evolution (Feigelson & Montmerle 1999).

PMS X-ray emission is elevated $10^1$ to $\gtrsim 10^4$ times above typical main sequence levels for stars with masses $0.1 M_\odot \lesssim M \lesssim 2 M_\odot$. High-amplitude X-ray variability and hard spectra, supported by multiwavelength studies such as photospheric Zeeman measurements and starspot mapping, indicate that the emission is primarily attributable to solar-type magnetic flares where plasma is heated to high temperatures by violent reconnection events in magnetic loops. However, the empirical relationships between PMS X-ray emission and stellar age, mass, radius, and rotation differ from those seen among solar-type main sequence stars (Flaccomio et al. 2003b; Feigelson et al. 2003). We have an inadequate understanding of the astrophysical origins of this magnetic activity. It is also unclear whether or not the high energy radiation from magnetic flaring has important astrophysical effects. For example, it is possible that some planets form in disk regions that are rendered turbulent from MHD instabilities induced by PMS X-rays (e.g., Glassgold, Feigelson & Montmerle 2000; Matsumura & Pudritz 2003). X-rays from embedded stars may affect ambipolar diffusion, and thus future star formation, in the surrounding molecular cloud. X-ray images are also particularly effective in locating low mass companions around luminous young stars. There are thus a variety of astrophysical reasons to investigate the magnetic activity of young stars. Due to the wide range of activity levels and other properties, it is advantageous to study large samples of stars.

The nearest rich and concentrated sample of PMS stars is the Orion Nebula Cluster (ONC), also known as the Trapezium Cluster or Ori Id OB association. The OB members of the ONC illuminate the Orion Nebula (= Messier 42), a blister H II region at the near edge of Orion A, the nearest giant molecular cloud ($D \simeq 450$ pc). The ONC has $\simeq 2000$ members within a 1 pc ($8'$) radius sphere with 80% of the stars younger than 1 Myr (Hillenbrand 1997). It was the first young stellar cluster to be detected in the X-ray band (Giacconi et al. 1972) and non-imaging studies soon found that the X-ray emission is extended on scales of a parsec or larger (den Boggende et al. 1978; Bradt & Kelley 1979). Early explanations for the Orion X-rays included winds from the massive Trapezium stars colliding with each other or the molecular cloud, and hot coronae or magnetic activity in lower mass T Tauri stars. The *Einstein* (Ku & Chanan 1979), *ROSAT* (Gagné et al. 1995; Geier et al. 1995; Alcalá et al. 1996) and *ASCA* (Yamauchi et al. 1996) imaging

X-ray observatories established that both the Trapezium stars and many lower-mass T Tauri stars contribute to the X-ray emission.

But these early studies could detect only a modest fraction of the ONC stars due to the high stellar densities and heavy absorption by molecular material along the line of sight. These limitations are alleviated by NASA's Chandra X-ray Observatory (*Chandra*). Its mirrors provide an unprecedented combination of capabilities - a wide spectral bandpass and $\lesssim 1''$ spatial resolution - and are particularly well-suited to the study of crowded and absorbed clusters of faint X-ray sources. The ONC was thus intensively studied during the first year of the *Chandra* mission with several instrumental setups: the Advanced CCD Imaging Spectrometer (ACIS) in imaging mode (Garmire et al. 2000; Feigelson et al. 2002a,b, 2003) and as detector for the High Energy Transmission Grating Spectrometer (Schulz et al. 2000, 2001, 2003), and with the High Resolution Imager (HRI; Flaccomio et al. 2003a,b).

While many valuable results emerged from these early *Chandra* studies, it was recognized that more would be learned from a much deeper and longer exposure of the Orion Nebula region. We present here a unique $\sim 10$ day, nearly continuous observation of the Orion Nebula obtained during the fourth year of the mission, nicknamed the *Chandra* Orion Ultradeep Project (COUP). This paper describes the COUP observations (§2), the data reduction (§3), source detection and characterization (§4-9), and identification with previously known PMS stars (§10-11). We provide extensive machine-readable tables of the X-ray sources and properties, and an atlas of their location in the sky (§12). Other COUP papers will discuss various astronomical and astrophysical issues emerging from these observations.

## 2. Observations

The COUP combines six nearly-consecutive exposures of the Orion Nebula Cluster (ONC) spanning 13.2 days in January 2003 with a total exposure time of 838 ks or 9.7 days (Table 1). The observations were obtained with the ACIS camera on-board *Chandra*, which are described by Weisskopf et al. (2002) and Garmire et al. (2003). We consider here only results arising from the imaging array (ACIS-I) of four abutted $1024 \times 1024$ pixel front-side illuminated charge-coupled devices (CCDs) covering about $17' \times 17'$ on the sky. The S2 chip in the spectroscopic array (ACIS-S) was also operational, but as the telescope point spread function (PSF) is considerably degraded far off-axis, the S2 data are omitted from the analysis. The ACIS-I aimpoint and the roll angle for all six observations were kept constant (Table 1). All six observations were taken in Very Faint telemetry mode to improve the screening of background events and thus increase the sensitivity of the observations. The focal plane temperature was between $-119.5$ and $-119.7$ °C.

The observations were constrained to be performed in January to accommodate a single roll of about 311 degrees. The observational span of 14 days means that the spacecraft's nominal roll changes by about 14 degrees. Typically, off-nominal rolls of greater than $\pm 5^\circ$ are difficult to

accommodate. However in January of 2003 the tolerance was somewhat higher in the direction of the ONC. The observations were continuous with the exception of five passages through the Van Allen belts, during each of which ACIS is taken out of the focal plane for about 29 ks. The spacecraft used these passages to unload momentum so that no other science target was observed between Jan 8 2003 21:00 GMT and Jan 22 2002 02:00 GMT. The outcome of 9.7 days exposure in a 13.2 day period (73% efficiency) is the maximum efficiency achievable by the spacecraft given the current perigee of about 33,000 km.

The COUP observation period was also remarkable in having some of the quietest solar weather in the *Chandra* mission. This reduces instrumental background and makes the dataset truly exceptional for variability analysis. The Advanced Composition Explorer (ACE) spacecraft, which is used to monitor the solar wind near the Earth, never saw fluxes above 200 particles $\mathrm{cm}^{-2}$ $\mathrm{s}^{-1}$ $\mathrm{ster}^{-1}$ $\mathrm{MeV}^{-1}$ in the P3 channel ($112 - 187$ keV). *Chandra* observations are generally terminated when this rate exceeds 50,000 to prevent damage to the ACIS CCDs. All particle detectors associated with the on-board Electron Proton Helium Instrument (EPHIN) also reported some of their lowest background measurements during this period. Nonetheless some data were lost. The typical ONC observation included about 45,000 frames (3.2-sec exposures) from each of the five CCDs. Typically less than 10 frames (20 events) from each CCD were lost due to telemetry errors. However the final observation, ObsID 3498, lost about 40 frames ($\sim 80$ events) of the roughly 18,000 sent from each CCD.

## 3. Data Selection

The COUP data reduction and cataloguing procedure is diagramed in Figure 1. We outline in this section the first steps of data selection; see Appendix B of Townsley et al. (2003) for more details on many of these steps. Procedures were performed with *CIAO* software package version 2.3, *FTOOLS* version 5.2, *XSPEC* version 11.2, the Penn State CTI corrector version 1.16, and the *acis_extract* package version 2.33. The latter two tools were developed at Penn State[11].

Data reduction starts with Level 1 event files provided by the *Chandra* X-ray Center (CXC). First, we filter out events on the S2 chip. Second, likely cosmic ray and associated afterglow events are identified, but not removed, by taking advantage of the Very Faint telemetry mode. Third, employing the PSU CTI Corrector (Townsley et al. 2002), the data are partially corrected for CCD charge transfer inefficiency (CTI) caused mainly by radiation damage at the beginning of the *Chandra* mission. Fourth, the data are cleaned with filters on event "grade" (only ASCA grades 0,2,3,4,6 are accepted), "status," and "good-time interval" filters supplied by the CXC. Energies $< 500$ eV and background events with energies $> 10500$ eV are removed. Bad pixel columns with

[11]Descriptions and codes for CTI correction and *acis_extract* can be found at http://www.astro.psu.edu/users/townsley/cti/ and http://www.astro.psu.edu/xray/docs/TARA/ae_users_guide.html, respectively.

energies $< 700$ eV, left by the standard processing, are removed. Fifth, for each of the six COUP observations, individual correction to the absolute astrometry was applied based on several hundred matches between the preliminary *Chandra* and VLT point source catalogs (see §10). Along with reapplying the new aspect solutions to the data lists, the slight broadening of the PSF from the CXC's software randomization of positions was removed. Sixth, the tangent planes (x,y coordinate systems) of the five COUP observations were re-projected to match the tangent plane of the first observation (ObsId 4395), and all six files were merged into a single data event file.

For the purpose of source detection only, we eliminated flaring pixel events and events identified earlier using Very Faint mode that, when combined with random background events, can produce faint spurious sources. This cleaning operation reduced the background by $\sim 17\%$ but at the same time it removed $\sim 7\%$ of real photons from many bright sources. In the later source photon extraction stage (see Figure 1), we use an event list that retains these events so that source brightnesses are not underestimated.

Figure 2 shows the resulting images. Note the bright CCD readout streaks emanating from the brightest sources. In actuality, every source in the field produces similar readout streaks, producing a spatially variable background which must be considered when sources are detected. The chip gaps and bad pixel columns in the form of white stripes are also noticeable, as the images displayed here have not been corrected for the exposure map.

As a large fraction of PMS stars are expected to be in binary systems, some with separations comparable to the *Chandra* PSF, we have applied a subpixel event repositioning (SER) technique to improve the effective resolution of the ACIS detector. The SER procedure used here considers the "splitting" of charge between adjacent CCD pixels in an energy-dependent fashion (Li et al. 2004). We have applied SER to the merged exposure with cosmic ray afterglow events removed. We tested the results of SER by examining image quality for 100 COUP sources with $> 300$ counts located at off-axis angles $\theta \lesssim 3'$. A 36% improvement in the PSF full width at half maximum (FWHM) is achieved on-axis. As expected from the PSF broadening off-axis, the SER-induced improvement decreases to 31%, 21%, and 16% at $\theta = 1'$, $2'$, and $3'$ off-axis, respectively (see Figure 3).

## 4. Source Detection

As there is no single optimal procedure for identifying sources in such a rich *Chandra* field, trial source lists were prepared independently by two groups within the COUP team. The Penn State group used a wavelet transform detection algorithm implemented as the *wavdetect* program within the CIAO data analysis system (Freeman et al. 2002). The Palermo group used the Palermo

wavelet transform detection code, *PWDetect*[12]. Source detection procedures were carried out on both the original and SER-corrected images, and on images constrained to include only soft and only hard events.

### 4.1. Penn State Procedure

A *Chandra* imaging effective exposure map with units of ($cm^2$ s counts photons$^{-1}$) was made from the product of an aspect histogram *asphist* and an instrument map. The aspect histogram gives the amount of time the *Chandra* optical axis dwelled on each part of the sky, and is derived from the satellite aspect solution. The instrument map provides the instantaneous effective area across the field of view. It includes the detector quantum efficiency, non-uniformities across the face of a detector, mirror vignetting, and bad pixels.

To reduce unnecessary computation on high-resolution images far off-axis where the PSF is degraded, we constructed four $1024 \times 1024$ pixel scenes around the aimpoint with $0.25''$, $0.50''$, $1.00''$, and $1.44''$ pixels. An effective exposure map was created for each scene assuming a monochromatic incident spectrum with photon energy of 1.6 keV, the approximate energy at which the largest number of photons was detected. To improve sensitivity to faint sources with unusually soft or hard spectra, for each scene we produced energy band-limited images from the merged event list (cleaned of flaring events) in the total band ($0.5 - 8.0$ keV), soft band ($0.5 - 2.0$ keV), and hard band ($2.0 - 8.0$ keV). These images were produced from the original merged event list, for the event list with background removal based on Very Faint telemetry mode, and for the SER-corrected event list. Source detection was thus performed on 36 $1024 \times 1024$ images: three event lists, four spatial resolutions, and three spectral bands.

We ran *wavdetect* with the probability threshold $P = 10^{-6}$ which theoretically permits a few false positive detections in each image, and with $P = 10^{-5}$ which permits dozens of false positives. The wavelet scales were set between 1–2, 1–4, 1–8, and 1–16 pixels for the $0.25''$, $0.50''$, $1.00''$, and $1.44''$ scenes respectively. We then merged the catalogs, keeping only a single entry for each source by removing duplicate entries obtained from detections in lower-resolution images, if such entries existed. The sources were then visually examined, resulting in the rejection of 184 *wavdetect* sources. Most of these were spurious triggers lying on the readout trails or PSF wings of $\theta^1$C Ori or other very bright sources. The remainder appear to be random associations of events that did not resemble the local PSF. During this examination of the image 109 closely spaced and weak but likely sources were added to the PSU source list. The resulting combined and cleaned *wavdetect* source list has 1622 detections.

[12]Description and code for *pwdetect* are available at http://www.astropa.unipa.it/progetti_ricerca/PWDetect. For the COUP analysis, the code was modified to accommodate the large number of events, the conspicuous PSF wings due to bright sources, and events occurring during CCD readouts.

### 4.2. Palermo Procedure

*PWDetect* is the *Chandra* version of *wdetect*, a source detection code originally developed for *ROSAT*/PSPC data, based on wavelet transforms (Damiani et al. 1997a,b). It works directly on event files, instead of binned images, and computes wavelet transforms on a range of spatial scales, to be sensitive to point-like as well as moderately extended sources. Compared to the *ROSAT* version, the code has been improved in order to deal with *Chandra*'s extremely good spatial resolution, which implies a very sparse distribution of background counts around a source. This Poisson character of the background was taken into account in establishing the detection significance, using empirical formulae based on simulations as described in Damiani et al. (1997a). In the special case of COUP data, *PWDetect* was further refined to deal with the very large number of events, and, more importantly, with the presence of readout trails and conspicuous PSF wings, both highlighted by the presence of bright sources and responsible for scores of spurious detections if not accounted for. Readout trails are now automatically identified and statistically removed prior to detection, thus greatly reducing the number of spurious detections. The wings of bright sources are treated by suitably raising the detection threshold along the PSF wings. In this way, we are able to discriminate real from false detections even very close to the bright Trapezium stars.

For the COUP analysis, *PWDetect* was run on the merged event file restricted to events with energies between 300 and 7000 eV (the method was not applied separately to hard and soft bands) and after application of the VF-mode background filtering. The significance threshold was set at $5.0\,\sigma$. This number is not strictly the same as the signal/noise ratio, but is defined as the probability of source existence, expressed in Gaussian sigmas. Simulation of source-free background fields indicate that, at the chosen $5.0\,\sigma$ significance level, $\approx$10 spurious sources should be present due to Poissonian fluctuations. This is a good compromise: setting the threshold more conservatively at $5.5\,\sigma$, corresponding to $\approx$1 spurious detection, would result in detecting about 50 fewer sources, with a net loss of $\approx$40 real sources.

Our initial list of *PWDetect* sources for the original event list contained 1497 COUP sources. From visual examination, 62 sources were rejected along readout trails, 5 were rejected in the PSF wings of $\theta^1$C Ori, and 7 were flagged as tentative due to their weakness. Fifteen additional sources were clearly visible by eye but were missed by *PWDetect* due to proximity to other sources. This particularly occurs when two close sources far off-axis, where the PSF is elongated, mimic a single radially symmetric source. The same procedure applied to the SER-corrected event file produced an initial list of 1493 sources. Seven of these were deemed legitimate new sources and were added to the list. The final Palermo source list comprises 1452 detected sources.

### 4.3. Final COUP Source List

From 64 sources detected by *wavdetect* but undetected by *PWDetect*, 38 have significance greater than $5.0\,\sigma$ (i.e., significance threshold for *PWDetect*). Of those 38, 19 are double sources,

and another 19 are located at the regions of inhomogeneous exposure map (i.e., chip gaps, field edges, and bad pixel columns). The Palermo procedure emerged with 10 sources missed by the Penn State procedure, so the combined list has 1632 detections. Following photon extraction and local background determination for each source (§5), 16 of these sources were found to have $< 3$ net (i.e., background-subtracted) counts. We subjectively decided that such weak sources are unreliable and have placed them in a separate list of tentative sources. The resulting COUP source list of 1616 sources is presented in Table 2.

The column entries to Table 2 are as follows. Column 1 gives the running source number which will be used in this and other COUP papers. Sources are listed in order of right ascension. Column 2 gives the source name in IAU format Jhhmmss.s−ddmmss with the IAU designation CXOONCJ (*Chandra* X-ray Observatory Orion Nebula Cluster J2000). Columns 3 and 4 give source position for epoch J2000.0 in degrees. For sources with $\theta < 5'$, the positions are obtained from a simple centroiding algorithm within the *acis_extract* procedure. For sources located farther off-axis, the wavelet positions were improved by correlating the event distribution with PSF images using a matched-filter technique implemented by *acis_extract*. Column 5 gives each source's positional uncertainty in arcseconds. These are calculated within *acis_extract* as 68% ($1\,\sigma$) confidence intervals using the Student's $T$ distribution[13]. Column 6 gives the off-axis angle for each source in arcminutes.

Column 7 gives a flag indicating a variety of warnings and difficulties. A "u" denotes uncertain objects; these are very weak sources without stellar counterparts which satisfy the detection criteria but are subjectively not completely convincing. Seventy-four sources have "u" designations. A "d" refers to a double source, defined as two sources with overlapping 90% PSF contours. A "p" defines a possible piled-up source, when the surface brightness of the source exceeds a level of 0.003 counts $s^{-1}$ $pixel^{-1}$. A "t" indicates that a source region crosses a bright source readout trail. A "w" indicates that the source is located in the wings of any bright source with number of counts $> 20000$. An "x" indicates a region of inhomogeneous or low exposure map, where the source is located near or on chip gaps, bad pixel columns, or field edges. Sources designated "x" will have disturbed lightcurves.

Column 8 defines the type of the source detection. The first digit indicates the image on which *wavdetect* found the source: 1 = total band image, 2 = soft band image only, 3 = hard band image

[13]The Central Limit Theorem (see i.e., p.17 in Lyons 1991) says that the mean values of all possible samples of a given size N drawn from a particular population tend to cluster in a bell-shaped curve (like Gaussian) around the mean of the population from which the samples are drawn, and the standard deviation of such a set of sample means ($\sigma_{\overline{x}}$) is related to the standard deviation of the population ($\sigma$) as $\sigma_{\overline{x}} = \sigma/\sqrt{\mathrm{N}}$. The positions of N events extracted from the source region may be considered as a sample of size N out of the set of all possible samples of that size drawn from the parent population (i.e., a highly populated PSF, truncated by the extraction region). In the case where the parent population standard deviation is not known, a roughly 68% confidence interval for the population mean (i.e., statistical uncertainty on source position) would be $1.0 \times \mathrm{S}/\sqrt{\mathrm{N}}$, where S is the observed sample standard deviation. This is true for large N. For small samples the confidence interval becomes $t \times (\mathrm{S}/\sqrt{\mathrm{N}})$ where $t$ is the confidence level of Student's $T$ distribution, whose exact shape depends on N (see i.e., p.86 in Lyons 1991). For an infinite number of N the Student's $T$ distribution is the same as the Gaussian distribution.

only, and 4 = total band image with background filtered in Very Faint mode only. The great majority of sources (1522 of 1616) were found in the total band image; still 45 sources were found only in the soft band, and 36 only in the hard band. The second digit indicates the type of event list on which a source was detected using *PWDetect*: 1 = merged event list filtered in Very Faint mode, and 2 = merged SER corrected event list.

Column 9 indicates parameters of the detection procedure. The first digit refers to *wavdetect* where 1 = probability threshold $P = 1 \times 10^{-6}$ and 2 = probability threshold $P = 1 \times 10^{-5}$. A "1" in the second digit indicates that the source was detected with the *PWDetect* algorithm only. A non-zero entry in the third digit indicates that the source was found only by visual inspection. Here, "1" sources were found by both the Penn State and Palermo groups, "2" sources were found only by the Penn State group, and "3" sources were found only by the Palermo group. A total of 123 of the 1616 sources were found only by visual inspection.

Column 10 gives the source significance calculated by *acis_extract*, which indicates how many times the source's net (background-subtracted) counts exceed the uncertainty on that quantity SigAE = NetCts/$\sigma$(NetCts) (§5). Column 11 defines the probability of source existence, expressed in Gaussian sigmas calculated by *PWDetect*.

Columns 12 and 13 list the source counterparts from previous *Chandra* studies with the ACIS (Feigelson et al. 2002a) and HRC (Flaccomio et al. 2003a) detectors. Counterparts to earlier *Einstein*, *ROSAT*, and *ASCA* sources are given by Feigelson et al. (2002a).

Table 3 lists the 16 tentative sources which passed the Penn State and Palermo source detection criteria but did not have $> 3$ net counts after photon extraction. Here we give only positions. These possible sources are not discussed further in this paper. The photometry results for those very weak sources strongly depend on the way local backgrounds are chosen. By introducing manually selected local background (§5), we may improve their photometry and reconsider our preliminary decision on whether these are real or tentative sources. This work will be done in the future COUP membership paper, Getman et. al. (in preparation).

## 5. Photon Extraction

The *acis_extract* package is used to extract source photons, refine the accuracy of source positions, estimate local background, construct source and background spectra, compute redistribution matrix files (RMFs) and auxiliary response files (ARFs), construct lightcurves and time-energy diagrams, perform a Kolmogorov-Smirnov variability test, compute photometric properties, and perform automated spectral grouping and fitting. The reader is referred to the *acis_extract* Users Guide[14] for further details on the implementation of each step. The quantities derived in the photon

[14]Users Guide for *acis_extract* can be found online at http://www.astro.psu.edu/xray/docs/TARA/ae_users_guide/.

extraction stage are listed in Table 4, and we refer to the columns of this table in this section.

Selection of an optimal extraction region for each source is not a simple task; one seeks a balance between a larger region maximizing the source's signal and (for weak sources) a smaller region minimizing the background's signal. The size and shape of the extraction region vary greatly over the field of view and cannot be parametrized accurately by an analytical expression. *Acis_extract* treats these difficulties by extracting the events around the source centroid (initially, the *wavdetect* position) inside a polygonal contour of the local PSF, obtained with the CIAO tool *mkpsf*. The user need only specify the fraction of the enclosed energy desired for the extraction. For most sources, we chose to extract events from the polygonal contours of $\sim 87\%$ encircled energy using PSFs at the fiducial energy of 1.497 keV. For $\sim 250$ weak and crowded COUP sources, we chose smaller PSF contours ranging from 20% to 80% encircled energy.

While the ACIS-I instrumental background level is usually spatially invariant, it can change substantially across the COUP field due to the PSF wings and readout trails of the strong sources. We therefore adopt the procedure used in *acis_extract* for automatically measuring and subtracting a local background individually for each source. The background extraction region starts with a circular annulus where the inner radius circumscribes the $\sim 1.1 \times 97\%$ PSF polygon and the outer radius is set such that the background region accumulated $> 100$ events. These background events are obtained from a special background image that has excluded all events within the $\sim 1.1 \times 97\%$ PSF circles of all 1616 sources, so background events for one source are not corrupted by source events from neighboring sources.

*Acis_extract* can also accept a user-generated background to accommodate unusual sources. The local background region was manually adjusted for 57 weak sources located in crowded fields, near or on readout trails, or on PSF wings of bright sources. Improvement of the local background is shown in Figure 4 for the sample COUP source #780. The spectrum to the left is extracted with the automatically subtracted background $R_1$, while the spectrum to the right is more realistic, and obtained by subtracting the manually chosen background $R_2$. Even with such care, some faint sources may still have spectra that are corrupted by incorrect background subtraction.

Results from the photon extraction procedure appear in Table 4. The source counts tabulated in Column 3 give the number of counts in the total (0.5 - 8 keV) energy band extracted for each source (including background). Column 4 gives the number of background counts in the total band scaled to the extracted area corrected for small differences that may be present in the exposure maps of the source and background regions. The net or background-corrected counts appear in Column 5; this is the difference between Columns 3 (extracted source counts) and 4 (scaled local background counts). Columns 6 and 7 give the area of the extraction polygon in $0.5'' \times 0.5''$ pixels and the fraction of the PSF at the fiducial energy of 1.497 keV enclosed within the extracted area.

Spectral analysis requires calibration files (ARFs and RMFs) specifying the effective area and spectral resolution of the instrument at each source location as a function of energy. As the Penn State CTI corrector has been applied to the COUP event data (§3), there is no need to calculate

RMFs for each source individually. Given the source location on each CCD chip, we select the appropriate RMF from a standard suite provided with the CTI corrector.

Source-specific ARF files are then calculated using the energy grid specified in these RMFs (685 PI channels, or 410 energy bands). In cases where a source spans multiple CCDs due to satellite dithering, the ARFs were calculated for both CCDs and summed. A further correction to the ARFs is applied to account for the energy dependence of the source PSF that falls outside the extraction region. PSFs were constructed at five fiducial energies between 0.27 and 8.6 keV (0.277, 1.497, 4.510, 6.400, and 8.600 keV), the polygonal source extraction region was applied to each PSF, the PSF fraction was computed at each available energy, and the ARF was reduced by this PSF fraction curve. The ARF was also corrected for the hydrocarbon build-up on the ACIS filters using the correction curve supplied by the tool *acisabs*[15].

The "effective" exposure time at the source location is given in Column 8. This quantity is derived by normalizing the ratio of an average exposure map ("Ct_Fl") to the one obtained for the region with the maximum value of the exposure map. Specifically, Exp = (Ct_Fl/Ct_Fl$_{\rm max}$)$\times$838 ks, where 838 ks is the COUP "observed" exposure time (sum of all exposures in Table 1). This quantity summarizes the variation in the "depth" to which the sources were observed.

Column 9 gives the value of the exposure map averaged over the source region (Ct_Fl) in units of ($10^9$ counts s cm$^2$ photon$^{-1}$) and represents a conversion factor between a photon incident flux and detected counts.

The final eight columns of Table 4 provide a variety of non-parametric measures of the source flux and spectrum. Column 10 gives a rough estimate of the incident flux at the telescope aperture in units of (photons cm$^{-2}$ s$^{-1}$): IncFl = NetCts/ $<$ ARF $>$ /Exp. Note that this flux estimate becomes inaccurate when the spectrum is not flat over the total $0.5-8$ keV band covered by the ARF. Summing the fluxes computed over narrow energy bands will produce a more accurate result, and parametric spectral fitting (§7) should produce the most accurate flux estimates. Column 11 gives the background-corrected median photon energy MedE in the $0.5-8.0$ keV range. IncFl and MedE can be used together for estimating the luminosities of weak sources (say, NetCts $\lesssim 20$) for which nonlinear spectral fitting packages are ineffective (§9).

Columns $12-17$ describe three hardness ratios and their $1\,\sigma$ upper and lower statistical errors. The hardness ratios are defined by HR = (Cts$_{\rm h}$ − Cts$_{\rm s}$)/(Cts$_{\rm h}$ + Cts$_{\rm s}$) where subscripts "h" and "s" refer to a harder and softer band, respectively. For COUP, we define HR1 to reproduce the commonly used hardness ratio between the s = $0.5-2.0$ keV and h = $2.0-8.0$ keV bands, HR2 to highlight the softer part of the spectrum between s = $0.5-1.7$ keV and h = $1.7-2.8$ keV, and HR3 to measure the harder part of the spectrum between s = $1.7-2.8$ keV and h = $2.8-8.0$ keV. For each energy band, *acis_extract* computes the net counts corrected for the local background in the appropriate band. Confidence intervals encompassing 68% of the expected error, equivalent

[15]A description of the *acisabs* procedure can be found online at http://www.astro.psu.edu/users/chartas/xcontdir/xcont.html.

to $\pm 1\,\sigma$ in a Gaussian distribution, are estimated first by calculating upper and lower errors on total and background counts using Gehrels (1986) equations (7) and (12), and then propagating those errors to net counts using Lyons (1991) equation (1.31). We then propagate errors from net counts to upper and lower uncertainties on hardness ratios using the method in Lyons (1991). When net counts are negative in an energy band we clip them at zero (to ensure that hardness ratios are bounded by [-1,1]) and choose to set their lower errors to zero. In cases where the 68% confidence interval of soft band net counts contains zero (very hard sources) we consider the upper uncertainties on hardness ratios to be unreliable and do not report them, similarly we do not report the lower uncertainties on hardness ratios of very soft sources. When the 68% confidence interval of both bands contains zero counts we do not report hardness ratios, because their errors would be large.

## 6. Strong Sources with Photon Pile-up

A few dozen COUP X-ray sources are simultaneously sufficiently strong and close to the aimpoint with narrow PSFs to suffer photon pile-up. This occurs when two or more photons are incident on a single CCD pixel during a single 3.2 s CCD frame. Some of these pile-up events mimic cosmic rays and are rejected by the on-board computer, while others are telemetered as valid events but with spuriously high energies. While statistical reconstruction treatments of ACIS pile-up have been developed (Davis 2001; Kang et al. 2003), the approach adopted here is to discard events at the core of the point spread function, which are both spatially and spectrally distorted, and to use only ordinary, pile-up-free events in the outskirts of the PSF (Broos et al. 1998).

Our procedure is to extract events from circular annuli between radii $r_{in}$ and $r_{out}$ (the latter was usually fixed around the 99% enclosed energy contour) and to construct specialized ARFs associated with those annuli at the particular source location. The ARF correction is made using the *xpsf* tool developed by G. Chartas[16] which uses MARX simulated sources to establish the energy-dependent fraction of photons in the extracted annulus. The challenge is to find the smallest $r_{in}$ which gives the greatest number of counts available for later analysis without reducing the inferred source flux because of photon pile-up. The best $r_{in}$ was established for each source by repeated trials [17]. We found that the best $r_{in}$ typically occurs at a surface brightness of $\sim 1.2 \times 10^{-3}$ counts s$^{-1}$ pixel$^{-1}$ which roughly corresponds to a pile-up fraction of $\sim 2\%$, or when the flux profile reaches a plateau. This is seen in the top two panels of Figure 5 for the heavily piled-up COUP source #932. The left panel (a) presents the brightness profile with the dashed line marking the level of $\sim 2\%$ pile-up fraction and the right panel (b) presents the luminosity (flux $\times 4\pi D^2$) profile obtained from the spectral fits of consequently diminishing annuli.

---

[16]Description of the procedure based on the algorithm of *xpsf.pro* can be found online at http://www.astro.psu.edu/users/tsujimot/arfcorr.html.

[17]More information can be found at http://www.astro.psu.edu/xray/docs/TARA/ae_users_guide/pileup.txt.

Sixty-five strong and centrally concentrated COUP sources were examined in this fashion; these sources are flagged "p" in Table 2. Only 24 sources were found to require the annular extraction analysis with results given in Table 5. Those 24 piled-up sources are also flagged with "a" in Table 6 (see §7 below). All further analysis for them (photometry, spectroscopy, variability) was performed with the annular extracted events. It is particularly critical that variability not be studied using the central piled-up core of these sources: flares often saturate and can even appear as plateaus or sudden dips in the count rates. An example of this spurious result is shown in panels (c) and (d) of Figure 5, where panel (c) presents the lightcurve extracted from the usual extraction region including pile-up, while panel (d) shows the lightcurve from the optimal annular extraction region.

## 7. Spectral Analysis

A goal of the present study is to produce an *acceptable* spectral model for the 1616 sources to give reliable time-averaged broadband luminosities and preliminary characterization of intrinsic spectral properties and interstellar absorption. We recognize that the semi-automated approach here using the *acis_extract* package will often not produce the *best* spectral model. Other COUP studies will analyze selected sources in much more detail, studying interstellar absorptions, plasma elemental abundances, time-variations of temperatures, and so forth. We describe the *acis_extract* spectral analysis procedure here.

For each of the 1616 COUP sources, the CIAO tool *dmextract* is first called to create a HEASARC/OGIP-compatible Type I source spectrum over the energy range $0-10$ keV, or PI channel range $0-685$ compatible with the Penn State CTI-corrected RMFs. The BACKSCAL keywords in the source and background spectra are the integral of the exposure map over the source and background regions. An algorithm for grouping spectra was implemented using custom code inside *acis_extract*, rather than via the grouping tools in FTOOLS (*grppha*) or CIAO (*dmgroup*), in order to place the first and last grouping bin boundaries at specified energies so that the spectra examined always have the range $0.5-8.0$ keV. These boundaries are controlled by specifying PI $= 1:34$ (energy $< 0.5$ keV) for the first group and PI $= 549:685$ (energy $\geq 8.0$ keV) for the last group. For the intermediate channels PI $= 35:548$ of scientific interest, channels were grouped according to the following scheme: each group contains at least 5 events for sources with NetCts $< 100$, at least 7 events for $100 \leq$ NetCts $< 200$, at least 10 events for $200 \leq$ NetCts $< 500$, at least 20 events for $500 \leq$ NetCts $< 1000$, and at least 60 events for NetCts $\geq 1000$. Simulations show that biases to the inferred temperatures when $kT \geq 10$ keV and to the column densities when $\log N_H \leq 20.5$ cm$^{-2}$ may be present when groups have NetCts $\leq 10$ events (Feigelson et al. 2002a §2.8).

Automated spectral fitting is performed by *acis_extract* by spawning the *XSPEC* spectral fitting program (Arnaud 1996). In most cases, spectra fits were found with one- and two-temperature optically thin thermal plasma MEKAL models (Mewe 1991), assuming a uniform density plasma with 0.3 times solar elemental abundances (Imanishi, Koyama, & Tsuboi 2001; Feigelson et al.

2002a). While these fits are usually statistically successful, the assumptions are clearly astrophysically inadequate. Detailed studies of magnetically active stars show that many plasma components with a wide range of temperatures may be present, and that chemical fractionation associated with magnetic reconnection flaring can produce strongly non-solar elemental abundance distributions (e.g. Kastner et al. 2002; Audard et al. 2003). X-ray absorption was modelled using the atomic cross sections of Morrison & McCammon (1983) with traditional solar abundances to infer a total (mainly hydrogen and helium) interstellar column density, $\log N_H$, in units of (atoms cm$^{-2}$)[18]. Here again, the astrophysical situation may be more complex with untraditional elemental abundances or gas-to-dust ratios (Vuong et al. 2003).

Acceptable spectral fits were obtained by minimizing $\chi^2$ between the grouped ACIS spectra and the parametric plasma models. We starting the fitting process in two ways: fixed standard values of the model parameters ($\log N_H = 21.3$ cm$^{-2}$, $kT_1 = 1.0$ and $kT_2 = 3.0$ keV), and a grid of initial parameters. The final result was chosen by visual inspection using *acis_extract's* accessory tool *spectra_viewer*, based on three criteria. First, for sources with NetCts $\lesssim 200$, one-temperature plasma models were used if they fit. Second, for hard sources with median energy MedE $\gtrsim 2$ keV, a one-temperature model fit was again chosen to avoid the highly nonlinear interaction of an unseen soft component and uncertain interstellar absorption. Third, for the brighter and softer sources (MedE $\lesssim 2$ keV, NetCts $\gtrsim 200$), two-temperature plasma fits were typically needed to obtain good fits. Uncertainties to each spectral parameter are estimated by a $\Delta\chi^2_{min}+$ constant criterion using the *error* command in *XSPEC*.

Emission measures were calculated using the best-fit normalizations from XSPEC as EM $= 10^{14} \times$ norm $\times 4\pi$D$^2$. In cases of two-temperature fits, both emission measures for soft and hard components are provided.

We emphasize again that the resulting spectral parameters and their uncertainties are often not reliably determined, and that alternative models may be similarly successful. The greatest uncertainty in plasma temperatures and emission measures occurs for sources with high absorption, $\log N_H \simeq 22 - 23$ cm$^{-2}$. Here we have no direct knowledge of the soft emission which, in less absorbed sources, typically dominates the hard emission. Thus, our approach here may severely underestimate broadband $0.5-8$ keV luminosities of heavily absorbed sources, although luminosities in the hard $2-8$ keV band are more reliable.

A second common source of uncertainty occurs for strong COUP sources where two qualitatively different spectral models give similarly good values of $\chi^2$. Figure 6 shows a typical example;

[18]Three strong COUP X-ray sources with complex spectra required two absorption components to achieve an acceptable spectral fit (in *XSPEC*, this model is specified *wabs* × *mekal* + *wabs* × *mekal*). These column densities were, for the three sources respectively: $\log N_{H1} < 20$ and $\log N_{H2} = 22.3$ for COUP source #267; $\log N_{H1} = 21.6$ and $\log N_{H2} = 22.8$ for #578; and $\log N_{H1} \sim 20.9$ and $\log N_{H2} \sim 22.8$ for #948. These values are not reported in Table 6. It is not clear whether the two components are astrophysically real (e.g., an unresolved double source with different absorptions) or result from poor spectral model specification.

the left panel shows the solution with the lower energy $kT_1$ of $0.1-0.3$ keV and higher energy $kT_2$ of $1-2$ keV, while the right panel presents another solution with $kT_1 \sim 0.6-0.9$ keV, $kT_2 \sim 2-3$ keV. Such ambiguities in spectral parameters occur in $\sim 150$ bright COUP sources. We have chosen here to present the second class of solution that avoids the inference of a very luminous, heavily absorbed, ultra-soft ($kT_1 < 0.5$ keV) component. The errors in *XSPEC* parameters do not take into account the possibility that we have chosen the incorrect acceptable model.

The results of our spectral analysis are tabulated in Table 6. One-temperature spectral fit results are recorded for 980 COUP sources and two-temperature results for 563 sources. Spectral models for 73 sources with very poor statistics (NetCts $< 20$) are left blank. Columns 3 and 4 report the logarithm of the hydrogen column density and its $1\,\sigma$ error in cm$^{-2}$, obtained from the spectral fit. Fitted values with $\log N_H < 20.0$ cm$^{-2}$ are truncated at 20.0 because ACIS-I spectra are insensitive to differences in very low column densities. Columns 5 and 6 give the plasma energy and its $1\sigma$ error in keV; in cases of two-temperature fits, this is the energy of the soft component. Columns 7 and 8 give the plasma energy of the hard component and its $1\,\sigma$ error in two-temperature model fits. Fitted values with $kT > 15$ keV are truncated at 15 keV because the data can not discriminate between very high temperature values. Columns 9-12 report the emission measures and their $1\,\sigma$ errors in the units of cm$^{-3}$ for each temperature component. Columns 13 and 14 give the reduced $\chi^2_\nu$ for the overall spectral fit and degrees of freedom, respectively.

Details regarding the spectral fitting process for individual sources are provided by the flags in columns $15-16$. Column 15 marks sources where the model was formally inadequate, based on the null hypothesis probability $P_\chi$ of $\chi^2$ for the relevant degrees of freedom: "m" indicates a marginal fit with $0.005 \le P_\chi < 0.05$, and "p" a poor fit with $P_\chi < 0.005$. Column 16 presents a three-part flag giving details of the spectral modelling for each source. The first part gives the minimum number of events in each spectral group. The second part indicates whether two absorption components are needed (see footnote 18). The third part gives the number of plasma components used in the accepted fit, 1 or 2. A "g" indicates that the spectral result has been chosen from a grid of initial parameter values.

Column 17 is a conjunction of eight flags giving important information on source-specific spectral features and problems, some obtained from visual inspection of the spectral fit and the location of the source in the ACIS image. The first flag "l" indicates the presence of narrow spectral features in the data that are not present in the model, probably due to elemental abundances inconsistent with our assumption of 0.3 $\times$ solar values. A total of 186 COUP sources are flagged with spectral features. Flags 2 and 3 indicate that soft ("s") or hard ("h") excesses were present in the data that were not in the model. In most cases, this can be attributed to poor subtraction of nonuniform local background around weak sources. The fourth flag "c" signals that the spectrum may be corrupted by a close star component. The fifth flag "p" indicates that the spectral fit is unreliable due to poor statistics and/or a poor fit based on visual examination rather than $\chi^2$ values. The sixth flag "m" marks cases where we defined the background extraction region with a manual (rather than automatic) procedure (§5). The seventh flag "a" marks the 24 heavily piled-up

sources requiring annular extraction, as discussed in §6. The eighth flag "w" notes 26 additional sources that appeared weakly piled-up for which the usual whole polygonal extraction region was used.

## 8. Variability Analysis

The temporal behaviors of COUP sources are often very complex with high-amplitude, rapidly changing flares superposed on quiescent or slowly variable emission. Relegating detailed study of these behaviors to later studies, we provide here two broadly applicable measures of variability and report results in Table 7. All variability measures are made on the extracted SrcCts events without background subtraction. While the background is usually negligible and is not itself highly variable, it may play a role in the variability characteristics of off-axis weaker sources. In 33 cases when sources were located on an ACIS CCD chip gap (flagged in column 3 of Table 7), tests have been performed on data extracted from the primary CCD only. These sources may exhibit spurious short-term variability. We are confident that the intrinsic variability of piled-up sources is accurately reflected by our annular extraction procedure (§6) though with reduced signal.

First, the *acis_extract* package applies the nonparametric one-sample Kolmogorov-Smirnov (KS) test to establish whether variations are present above those expected from Poisson noise associated with a constant source. Here the cumulative distribution of photon arrival times is compared to a simple model for a constant source subject to the same gaps in observation times due to orbit perigees (Figure 7a). In Table 7 Column 4 reports the logarithm of test significance: probability values $\log P_{\rm KS} \leq -3.0$ can be considered almost definitely variable, while variability has not been reliably detected when $\log P_{\rm KS} > -2.0$. Log $P_{\rm KS}$ has been truncated at $-4.0$ for strong sources with high amplitude variability because the tail of the statistic distribution is not well-defined.

Second, we employed the Bayesian Block (BB) parametric model of source variability developed by Scargle (1998). Here, the lightcurve is segmented into a contiguous sequence of constant count rates (Figure 7b). The change points between constant count rates are determined by an iterative maximum likelihood procedure for a Poissonian process. We modeled the ACIS frame mode data stream as binned data, with modifications to cancel the COUP bad time intervals. The maximum likelihood procedure corresponding to binned data was implemented in the IDL language[19]. BB constant count rates and boundaries were corrected for CCD readout dead times and COUP bad time intervals, respectively. The prior ratio parameter indicates the subjective preference we have for the single-rate Poisson model over the dual-rate model prior to analyzing the data. This quantity is practically useful for suppressing spurious segments due to the statistical fluctuations. We found that the overall shape of the BB light curves is insensitive to large changes in the prior ratio, from

[19]Description of this procedure and code can be found online at http://www.astro.psu.edu/users/gkosta/COUP/BBCODE/.

1 up to the ratio of the length of data interval to the desired time resolution for bright COUP sources ($\sim 100 - 200$), that is the condition to stop oversegmenting (Scargle 1998). Thus the prior ratio parameter was assigned the unbiased value of 1.

A more important parameter is the minimum number of counts allowed in a segment, which stops the segmenting process; in many cases, the number of segments varies with this value. After experimentation, we chose a minimum of 5 counts per segment in order to achieve maximal consistency between the BB and KS tests for marginally variable sources. Specifically, if we define a source to be BB variable if the number of segments BBNum $\geq 2$ and a source to be KS variable if $\log P_{\rm KS} < -2.0$, then 1515 of 1616 COUP sources are consistently classified as variable or non-variable by the two methods. With these criteria for variability, 60% (974 for KS or 973 for BB) of the 1616 COUP sources are variable. One consequence of combining the unbiased prior ratio parameter with only 5 minimum counts per segment is that strong sources often trigger isolated short segments with a small count number. These spurious peaks are easily identified by visual examination of the BB light curve.

Columns $5 - 9$ of Table 7 report the results of the BB variability analysis. They give the number of segments BBNum, the count rates of the lowest and highest segments, and their $1\,\sigma$ uncertainties (from Gehrels 1986) assuming Poisson statistics within the segment. The minimum count rate might sometimes be viewed as the quiescent level between flaring events. The ratio of maximum to minimum count rates may, within errors, be viewed as a measure of variability amplitude. We caution, however, that visual examination and individual analysis of lightcurves is needed for a full understanding of COUP source variability.

## 9. Luminosities

X-ray luminosities are provided here in three broad bands: $L_s$ in the soft $0.5 - 2.0$ keV band; $L_h$ in the hard $2.0 - 8.0$ keV band; and $L_t$ in the total $0.5 - 8.0$ keV band. Luminosities are calculated from fluxes $F$ in these bands according to $L = 4\pi D^2 F$ assuming a distance $D = 450$ pc to the Orion Nebula region. For 1543 of the 1616 COUP sources, fluxes are obtained from the thermal plasma spectral fits (§7) using *XSPEC's flux* tool which integrates the model spectrum over the desired band. Since the ARFs used with *XSPEC* incorporate instrumental effects, such as the unextracted PSF fraction and absorption by hydrocarbon contamination on the detector, no additional correction factors are needed at this stage. Running *XSPEC's flux* tool with the fitted plasma energies and emission measures but with zero absorption gives estimates of the intrinsic source emission prior to interstellar absorption. We call these absorption-'corrected' luminosities $L_{s,c}$, $L_{h,c}$ and $L_{t,c}$. Formal $\sqrt{N}$ statistical uncertainties on the luminosity can be readily obtained from NetCts and HR1 values in Table 4. For most sources, these statistical uncertainties to the luminosities are only about $\pm 0.1$ or less in $\log L$.

The scientific reliability of these luminosities, however, is usually considerably lower than

the formal statistical uncertainty for several reasons. First, 60% of the sources exhibit temporal variability, often by factors of 0.3−1.3 in $\log L_t$ (§8). Second, the measured value of $L_s$ is often only a small fraction of the emitted soft luminosity due to interstellar absorption. There are $> 300$ sources with fitted $\log N_H \geq 22.5$ cm$^{-2}$; for such heavily absorbed sources, the soft plasma component and $L_s$ is essentially unknown from spectral fits. The average lightly absorbed source has $L_s \simeq 2L_h$, so that the majority of the luminosity is probably missed in the heavily absorbed sources. The absorption-corrected value $\log L_{s,c}$ is so uncertain that we do not provide it for scientific analysis.

For the 73 faintest sources without any *XSPEC* spectral fit, we estimate the total band luminosities $\hat{L}_t \propto \mathrm{IncFl} \times \mathrm{MedE}$, where the incident flux IncFl and source's median energy MedE are given in Table 4. The basis for this approximation is the strong correlation between the $\log L_t$ values derived from the *XSPEC* spectral fits with the approximate $\hat{L}_t$ values shown in Figure 8. These values generally differ from each other by no more than 0.2 in $\log L$.

Columns $3-7$ of Table 8 list $\log L_s$, $\log L_h$, $\log L_{h,c}$, $\log L_t$ and $\log L_{t,c}$.

## 10. Stellar Counterparts

COUP source positions were compared with source positions from two optical catalogs, two near-infrared ($JHK_s$ bands) catalogs, and two thermal-infrared ($L$ band) catalogs. These catalogs differ in sensitivity and fields of view. In the optical band, we use the catalog of Hillenbrand (1997, henceforth H97) and additional stars found by Herbst et al. (2002, henceforth H02). Both of these surveys cover the full COUP field. In the $JHK_s$ bands, we use a merged catalog developed by McCaughrean et al. (in preparation; henceforth McC04) for the inner, most sensitive quarter of the COUP field and the 2 Micron All-Sky Survey (Cutri et al. 2003, henceforth 2MASS) for the outer portions of the field. Many of the 2MASS nondetections (i.e., 2MASS sources not detected in the COUP image) can be attributed to spurious sources in the 2MASS catalog which lie along bright emission-line filaments of the nebula (such as the Orion Bar). In the $L$-band, we use the catalog of Lada et al. (2004, henceforth LMLA) for a small inner region and the catalog of Muench et al. (2002, henceforth MLLA) for additional coverage around the center of the COUP field.

The $JHK_s$ catalog provided by McC04 is particularly valuable for studies in the inner $7' \times 7'$ of the COUP field. It starts with a deep imaging survey of the inner Trapezium Cluster made using the ISAAC near-infrared camera on UT1 of the ESO Very Large Telescope which reaches $5\sigma$ point source limiting magnitudes of approximately 22, 21, and 20, at $J_s$, $H$, and $K_s$, respectively. The seeing is roughly 0.5–0.6 arcsec FWHM throughout and thus a good match to the ACIS PSF in this inner crowded region. Its 1204 point sources are astrometrically tied to the 2MASS reference frame with $0.15''$ root-mean-squared accuracy. As the VLT data are saturated for sources brighter than ∼13 magnitudes in all filters, magnitudes for brighter stars were from other wide-field ONC catalogs and high spatial resolution studies of the inner core region as necessary (McCaughrean & Stauffer 1994; Hillenbrand 1997; Petr et al. 1998; Simon, Close, & Beck 1999; Lucas & Roche

2000; Luhman et al. 2000; Muench et al. 2002; Schertl et al. 2003, and 2MASS). Care was taken to place all of the photometric data on the 2MASS $JHK_s$ color system as far as possible, resulting in a homogeneous merged catalog covering the brightest OB stars down to candidate 3–5 $M_{Jup}$ proto-brown dwarfs in this inner region.

For each catalog, we performed automated cross-correlations between COUP and catalog source positions within a search radius of $1''$ for COUP source within $\simeq 3.5'$ of the field center, and within a search radius of $2''$ in the outer regions of the field where the *Chandra* point spread function deteriorates. The results of this search are given in Tables 9 and 10.

To evaluate the merits of this automatic procedure, we performed a careful visual examination of each COUP source. In ≃98% of the cases, the identifications are clear and unambiguous. Median offsets between COUP sources and near-infrared stars are only $0.15''$, and between COUP and optical stars are only $0.24''$[20] indicating superb astrometric positions in the COUP field. Figure 9 shows individual offsets as a function of off-axis angle; median offsets are better than $0.2''$ at the central part of the field and $0.4''$ at larger off-axis angles. Note that the (unexplained) deterioration of several arcseconds in off-axis positions reported by Feigelson et al. (2002a) in earlier Orion ACIS data is not present in COUP positions.

But in a few dozen cases, stellar identifications are complicated due to closely spaced stars, many of which are probably physical binaries. In some cases, a single COUP source spans double NIR and/or optical systems (see notes on individual sources in electronic versions of Tables 9 and 10), while other cases have double COUP sources with a single optical/infrared star. In the former case, the closest optical/IR source is tentatively assigned to a COUP source; in the latter case, either the same optical/infrared counterpart is assigned to two COUP sources (if the 90% PSF contours both encompass the optical/IR position) or an optical/infrared counterpart is tentatively assigned to the closest COUP source. These cases, and other situations where stellar identifications may be insecure, will be discussed separately in Getman et al. (in preparation). The listings in Tables 9 and 10 are thus probable, and not necessarily confirmed, physical associations between COUP sources and previously identified stars.

In the inner region covered by the deep VLT survey, there are a total of 883 COUP sources detected, 738 of which have stellar counterparts in the McC04 merged catalog. However, that catalog contains a total of 1204 stellar sources in the same region, indicating that the COUP detection rate of cluster members is ∼61%. The great majority of these non-recovered sources are faint, low-mass members of the cluster, most of which lie in the brown dwarf regime. A careful discussion of the reasons for this fall-off in COUP detections at the lowest masses and their consequences for the X-ray activity of brown dwarfs will be given in a future paper.

We find that 273 (17% of 1616) COUP sources are not identified with any of the known

[20]Hillenbrand's positions have been shifted by $+0.78''$ in right ascension and -0.38″ in declination from the original publication.

optical/IR sources. Nearly 90% of these are hard sources with MedE $> 2$ keV, which is a clear indicator of heavy absorption, and they constitute nearly 40% of all hard COUP sources. However, by itself, this does not determine which of these unidentified sources are new PMS stars associated with the Orion molecular cloud and which are background (primarily extragalactic) sources.

For the probable optical stellar counterparts in Table 9, the star identifier is given in Column 3 where designations between 0 and 9999 are from H97 and 10000-11000 are from H02. Column 4 gives the offset between the optical and COUP positions. The remaining 15 columns provide optical measurements and inferred stellar properties based largely on the comprehensive study of H97. Columns $5-6$ give $V$ and $I$ magnitudes from H97. Spectral types in Column 7 are from H97 updated with the work of Luhman et al. (2000) and Lucas et al. (2001). Effective temperatures (Column 9) are based on spectral types following Hillenbrand & White (2004), while visual absorption $A_V$ (Column 8), bolometric luminosity $\log L_{\rm bol}$ (Column 10), and radius $R$ (Column 11) are derived as in H97. Columns 12 and 13 are the mass $M$ and age $\log t$ recalculated by us using the PMS evolutionary tracks of Siess, Dufour, & Forestini (2000). Users should be cautious when using the intrinsic stellar properties as they are less accurate than the precision given in the tables. Errors arise from intrinsic photometric variability, uncertainties in spectral types and conversions to effective temperatures and bolometric luminosities, and, for the mass and age estimates, uncertainties in theoretical evolutionary tracks (see Hillenbrand & White 2004).

Columns $14-15$ give two properties associated with circumstellar material and accretion measured by Hillenbrand et al. (1998): the $K$-band excess attributable to a hot circumstellar disk, $\Delta(I-K)$, and the equivalent width of the Ca II infrared triplet lines with $\lambda = 8542\mathring{A}$, $EW$(Ca). A negative value here represents an emission line. Columns $16-19$ give properties derived from $\sim 90$ epochs of photometric monitoring by H02: the average $V$ magnitude $< V >$ and its standard deviation $\Delta V$, the range in $V$ about this mean, and the rotational period $P$ derived from periodicity attributed to rotationally modulated starspots.

Individual near-infrared counterparts for COUP sources are listed in Table 10 along with infrared properties. Column 3 gives the source identifier obtained from the merged catalog of McC04 for the inner region of the COUP field, and the 2MASS designation for the outer region. The positional offsets and $JHK_s$ magnitudes from the appropriate catalog appear in columns $4-7$. Column 8 gives a flag for McC04 sources indicating the source of the photometry: 1 from the VLT; 2 and 3 from the NTT and FLWO surveys, respectively, presented by Muench et al. (2002); 4 from the compilation of H97, and 5 from 2MASS or other sources. Columns $9-10$ give flags for 2MASS sources. The values of the photometry quality flag in column 9 are: A = signal-to-noise ratio (SNR) $\geqslant 10$; B = SNR $\geqslant 7$; C = SNR $\geqslant 5$; D = low significance detection; E = PSF fitting poor; F = reliable photometric errors not available; X = source detected but no valid photometry is available. The values of the confusion and contamination flag in column 10 are: 0 = no problem; b = possible multiple source; c = photometric confusion from nearby star; d = diffraction spike confusion from nearby star; p = persistence contamination from nearby star; and s = electronic stripe from nearby star.

Columns 11 − 13 of Table 10 refer to L band data. The first column indicates whether the photometry is obtained from the surveys of Muench et al. (2002, designated M) or Lada et al. (2004, designated L). The second column gives the running source number from the L band catalog. The final column gives the L magnitude.

## 11. Nondetections of Cluster Members

Tables 11−12 provide lists of upper limits for the Hillenbrand (1997) $V < 20$ optical catalog and the 2MASS $K < 15$ near-infrared catalog. The first three columns in the tables give object identification name or number and star position from the associated catalog. The next three columns give information from the COUP image: the upper limit on the number of counts at that position, effective exposure time at the object position, and a confusion flag if the object is influenced by nearby sources. The remaining columns reproduce catalog optical and near-infrared properties for the stars (see §10). We underscore the importance of the contamination and confusion flags in the 2MASS dataset, as a considerable number of 2MASS cataloged sources are small-scale bright spots in the diffuse nebular emission rather than true stars.

The upper limits to the COUP counts for these sources were calculated using *PWDetect* and are therefore consistent with the *PWDetect* detection procedure. They indicate the minimum source counts required, for a detection using *PWDetect* at a significance level of $5.0\,\sigma$, i.e., the same used for detection. Our final source list contains some sources with fewer counts than the upper limits derived by *PWDetect*. This can be due to: 1) the use of other detection methods, which can, in some situations, be more sensitive than *PWDetect* (e.g., the eye is able to detect a faint source close to a bright one more easily than a wavelet based detection algorithm, especially where the PSF is azimuthally distorted); 2) random fluctuations in the spatial distribution of source events raising the S/N of a source above the detection threshold. Such a source would be undetectable if it had a nominal PSF.

For most stars, the upper limits are estimated analytically from the source-free background map computed by *PWDetect*. In many cases where the undetected stars lie on PSF wings of a detected source (as indicated by the flag in Tables 11−12), the analytical method may significantly overestimate upper limits. More stringent limits were derived for such sources by adding test sources at a variety of count levels at the upper limit position in the ACIS image. The wavelet transforms of these simulated images were then examined to determine the minimum count level (reported as the upper limit in our tables) at which the simulated source becomes detectable (i.e., produces a second peak next to that of the detected source).

It is often desirable to estimate the luminosity upper limits and we include a possible procedure below (these luminosity upper limits will be included in a future COUP publication). Derive an upper limit to the count rate as LimCt/Exp using Tables 11−12, calculate $N_{\rm H}$ according to the formula $N_{\rm H}({\rm cm}^{-2}) \sim A_V({\rm mag}) \times 1.6 \times 10^{21}$ (Vuong et al. 2003), use PIMMS to compute the

unabsorbed flux from the count rates assuming an optically thin plasma spectrum with $kT \sim 1$ keV. Although the mean temperature of the detected COUP sources is somewhat higher than 1 keV, there is a trend of increasing temperature with increasing X-ray luminosity, and since we can expect the undetected objects to be more similar to the faintest X-ray sources, 1 keV should be a reasonable value.

## 12. Maps and Source Atlas

Figure 11 provides closeup maps covering the entire merged COUP ACIS-I field with 1616 COUP sources labelled. The field was divided into 29 panels with the innermost panel having the highest resolution. A guide to the map panels is provided in Figure 10; this guide also gives the pixel size for each panel. The plotted intensities are scaled to the log of the photons in each pixel.

The *acis_extract* package also produces an "atlas" where both tabulated and graphical information on each source is collected onto a single page. Figure 12 shows a sample page. The graphs display various projections of the four-dimensional ACIS dataset – photons as a function of RA, Dec, energy, and time – with ancillary plots associated with our spatial, spectral, and variability analysis[21].

After the COUP source name, the upper panel of each atlas page shows the lightcurve of extracted events without background subtraction. In the few cases where the source lies near a gap in the CCD array, it covers only the primary CCD. The abscissa is in hours from the start of the observation and the ordinate is in counts $\mathrm{ks}^{-1}$. The black histogram shows the total $0.5-8.0$ keV energy band, while the red lines show the soft ($0.5-2.0$ keV) and the blue lines show the hard ($2.0-8.0$ keV) energy bands. The light curve binning depends on source strength according to the following scheme: SrcCnts $< 200$, bin width $= 6.3$ hours; $< 500$, 3.2 hours; $< 10000$, 1.6 hours; $< 20000$, 1.1 hours; $< 40000$, 47.6 minutes; and $\geq 40000$, 23.8 minutes.

The second panel presents the photon arrival times as a function of energy in the total energy band. The overplotted lines represent the cumulative distributions of data (red) and uniform model (green), used to compute the K-S variability test (§8).

The bottom left and center panels show the raw and adaptively smoothed images around the source. The images subtend $50.5'' \times 50.5''$ size with $0.25''$-pixel bins oriented with north at the top and east to the left. Brightness is scaled to the logarithm of counts in each pixel; isolated individual events are always visible in the raw image. The raw image shows a green polygon representing the *acis_extract* source extraction region and a red circle representing the source mask used in construction of the Penn State background map ($1.1 \times 97\%$ PSF region). Small colored symbols indicate the location of IR and optical sources: cyan + are from VLT $JHK$ catalog, yellow

[21]The 1616 pages of the COUP atlas are available in PDF format at http://www.astro.psu.edu/users/gkosta/COUP/DATA_PRODUCTS_08_17_04/ATLAS/.

circles are from the 2MASS $JHK_s$ catalog, blue × are from the MLLA $JHKL$ catalog, and red boxes are from the optical catalog of Hillenbrand (1997). The adaptive smoothing is performed using the CIAO tool *csmooth* at the $2.5\sigma$ level. The adaptively smoothed image in the center panel is a "true-color"[22] X-ray image where red represents the $0.5 - 1.7$ keV band counts, green the $1.7 - 2.8$ keV counts, and blue the $2.8 - 8.0$ keV counts.

The bottom right panel of each atlas page shows the extracted source spectrum after background subtraction and the chosen model from the *XSPEC* spectral fitting procedure (§7 and Table 6). The top plot shows the source spectrum after grouping as separated lines with error bars and a continuous step-function representing the fitted model. The abscissa is in units of log (keV) and the ordinate is in units of log (cts $s^{-1}$ $keV^{-1}$). The bottom plot shows residuals in units of contribution to the $\chi^2$ statistic.

Finally, below the figures on each page of the COUP atlas we collect many of the X-ray positional, photometric, spectral, variability, and stellar counterpart quantities given in Tables 2 - 8.

## 13. Summary

This paper presents the observations, data analysis methodology, and tabulated results for the *Chandra* Orion Ultradeep Project. We describe techniques used in the COUP data reduction, derivation of time-averaged source properties, and production of the source catalog. The results of this study are the tables of the 1616 COUP source properties (Tables 2, 4, 6, 7, 8, 9, and 10), tables of undetected sources (Tables 11 and 12), map of the field (Figure 11), and the 1616 page atlas detailing the analysis and findings for each source.

Our data reduction procedure seeks to use the most well-developed methods available for the identification and extraction of point sources in *Chandra* ACIS images. The source detection procedure is based on two wavelet-based search algorithms, run on datasets constructed in several bands, supplemented by visual inspection of the image. The dataset is optimized for maximum reduction of background and maximum spatial resolution with subpixel event repositioning. We identify 1616 X-ray sources in the $\sim 17' \times 17'$ ACIS-I field.

For each source, we perform data extraction, pile-up analysis, spectral analysis, variability analysis, and broad-band luminosity determinations using the sophisticated semi-automated IDL-based *acis_extract* package. The algorithms used in *acis_extract* successfully address many difficulties

[22]Red, green, and blue images are scaled using a color model (from the TARA package http://www.astro.psu.edu/xray/docs/TARA/) that preserves the "hue" of the data (ratios among red, green, and blue signals), even for regions where the brightness is saturated. The color white and other shades of grey appear only where the red, green, and blue signals are approximately equal. A similar technique has been described by Lupton et al. (2003).

related to the COUP observation such as the position-dependent point spread function, multiple exposures with different pointings and time gaps, source crowding, piled-up sources, nonuniform local background and exposure map, and so on. Our treatment of photon pile-up for strong sources using annular extraction regions is first used here in a formal procedure. The *acis_extract* package, which is available to the public, can be used to create point source catalogs for many *Chandra* studies.

These images, atlases and tables serve as the foundation for various studies of the COUP observations. These will include investigation of X-ray emission from different classes of pre-main sequence stars: OB, intermediate-mass, T Tauri and brown dwarfs; deeply embedded stars which are often younger protostars; and binary and multiple star systems. We will also investigate the astrophysical issues such as the magnetic field generation and geometries in pre-main sequence systems, plasma energetics in powerful magnetic reconnection flaring events, and X-ray ionization of circumstellar disks and cloud material. Altogether, the COUP data products presented here offer the most detailed and comprehensive information to date concerning the X-ray emission and magnetic activity in pre-main sequence stars.

We thank George Chartas (Penn State) for providing the ARF correction tool, *xpsf*, and acknowledge the unusual efforts of the *Chandra* Mission Operations group in scheduling the COUP observations. We also thank the referee, M. Muno, for his time and many useful comments that improved this work. COUP is supported by *Chandra* guest observer grant SAO GO3-4009A (E. D. Feigelson, PI). This work was also supported by the ACIS Team contract NAS8-38252, HRC Team contract NAS8-39073. EF, FD, GM and SS acknowledge financial contribution from Italian MIUR (COFIN-PRIN 2001) and from INAF. MJM and G. Meeus acknowledge support from the European Commission Research Training Network "The Formation and Evolution of Young Stellar Clusters" (HPRN-CT-2000-00155). This publication makes use of data products from the Two Micron All Sky Survey, which is a joint project of the University of Massachusetts and the Infrared Processing and Analysis Center/California Institute of Technology, funded by the National Aeronautics and Space Administration and the National Science Foundation.

## REFERENCES

Alcalá, J. M. et al. 1996, A&AS, 199, 7

Arnaud, K. A. 1996, in Data Analysis Software and Systems V, ed. G. H. Jacoby & J. Barnes (San Francisco:ASP), 17

Audard, M., Güdel, M., Sres, A., Raassen, A. J. J., & Mewe, R. 2003, A&A, 398, 1137

Bradt, H. V. & Kelley, R. L. 1979, ApJ, 228, L33

Broos, P. S., Townsley, L. K., & Nousek, J. A. 1998, Proc. SPIE, 3444, 30

Cutri, R. M. et al. 2003, VizieR Online Data Catalog, 2246

Davis, J. E. 2001, ApJ, 562, 575

den Boggende, A. J. F., Mewe, R., Gronenschild, E. H. B. M., Heise, J., Grindlay, J. E., 1978, A&A, 62, 1

Damiani, F., Maggio, A., Micela, G., & Sciortino, S. 1997a, ApJ, 483, 350

Damiani, F., Maggio, A., Micela, G., & Sciortino, S. 1997b, ApJ, 483, 380

Feigelson, E. D. & Montmerle, T. 1999, ARA&A, 37, 363

Feigelson, E. D., Broos, P., Gaffney, J. A., Garmire, G., Hillenbrand, L. A., Pravdo, S. H., Townsley, L., & Tsuboi, Y. 2002a, ApJ, 574, 258

Feigelson, E. D., Garmire, G. P., & Pravdo, S. H. 2002b, ApJ, 572, 335

Feigelson, E. D., Gaffney, J. A., Garmire, G., Hillenbrand, L. A., & Townsley, L. 2003, ApJ, 584, 911

Flaccomio, E., Damiani, F., Micela, G., Sciortino, S., Harnden, F. R., Murray, S. S., & Wolk, S. J. 2003, ApJ, 582, 382

Flaccomio, E., Damiani, F., Micela, G., Sciortino, S., Harnden, F. R., Murray, S. S., & Wolk, S. J. 2003b, ApJ, 582, 398

Freeman, P. E., Kashyap, V., Rosner, R., & Lamb, D. Q. 2002, ApJS, 138, 185

Gagné, M., Caillault, J.-P. & Stauffer, J. R. 1995, ApJ, 445, 280

Geier, S., Wendker, H. J. & Wisotzki, L. 1995, A&A, 229, 39

Garmire, G., Feigelson, E. D., Broos, P., Hillenbrand, L. A., Pravdo, S. H., Townsley, L., & Tsuboi, Y. 2000, AJ, 120, 1426

Garmire, G. P., Bautz, M. W., Ford, P. G., Nousek, J. A., & Ricker, G. R. 2003, Proc. SPIE, 4851, 28

Gehrels, N. 1986, ApJ, 303, 336

Giacconi, R., Murray, S., Gursky, H., Schreier, E., Tananbaum, H. 1972, ApJ, 178, 281

Glassgold, A. E., Feigelson, E. D., & Montmerle, T. 2000, in Protostars and Planets IV, 429

Herbst, W., Bailer-Jones, C. A. L., Mundt, R., Meisenheimer, K., & Wackermann, R. 2002, A&A, 396, 513

Hillenbrand, L. A. 1997, AJ, 113, 1733

Hillenbrand, L. A., Strom, S. E., Calvet, N., Merrill, K. M., Gatley, I., Makidon, R. B., Meyer, M. R., & Skrutskie, M. F. 1998, AJ, 116, 1816

Hillenbrand, L. A. & Carpenter, J. M. 2000, ApJ, 540, 236

Hillenbrand, L. A. & White, R. J. 2004, ApJ, 604, 741

Imanishi, K., Koyama, K., & Tsuboi, Y. 2001, ApJ, 557, 747

Kang, H., van Dyk, D. A., Yu, Y., Siemiginowska, A., Connors, A., & Kashyap, V. L. 2003, in Statistical Challenges in Astronomy, E. D. Feigelson & G. J. Babu (eds.), 449

Kastner, J. H., Huenemoerder, D. P., Schulz, N. S., Canizares, C. R., & Weintraub, D. A. 2002, ApJ, 567, 434

Ku, W. H.-M. & Chanan, G. A. 1979, ApJ, 234, L59

Lada, C. J., Muench, A. A., Lada E. A., & Alves J. F. 2004, AJ, in press, astro-ph/0406326

Li, J., Kastner, J. H., Prigozhin, G. Y., Schulz, N. S., Feigelson, E. D., & Getman, K. V. 2004, ApJ, in press, (astro-ph/0401592)

Lucas, P. W. & Roche, P. F. 2000, MNRAS, 314, 858

Lucas, P. W., Roche, P. F., Allard, F., & Hauschildt, P. H. 2001, MNRAS, 326, 695

Luhman, K. L., Rieke, G. H., Young, E. T., Cotera, A. S., Chen, H., Rieke, M. J., Schneider, G., & Thompson, R. I. 2000, ApJ, 540, 1016

Lupton, R., Blanton, M. R., Fekete, G., Hogg, D. W., O'Mullane, W., Szalay, A., & Wherry, N. 2003, PASP, 116, 133

Lyons, L. 1991, A Practical Guide to Data Analysis for Physical Science Students (Cambridge: Cambridge Univ. Press)

Matsumura, S. & Pudritz, R. E. 2003, ApJ, 598, 645

McCaughrean, M. J. & Stauffer, J. R. 1994, AJ, 108, 1382

Mewe, R. 1991, A&A Rev., 3, 127

Morrison, R. & McCammon, D. 1983, ApJ, 270, 119

Muench, A. A., Lada, E. A., Lada, C. J., & Alves, J. 2002, ApJ, 573, 366

Petr, M. G., Coude Du Foresto, V., Beckwith, S. V. W., Richichi, A., & McCaughrean, M. J. 1998, ApJ, 500, 825

Scargle, J. D. 1998, ApJ, 504, 405

Schertl, D., Balega, Y. Y., Preibisch, T., & Weigelt, G. 2003, A&A, 402, 267

Schulz, N. S., Canizares, C. R., Huenemoerder, D., & Lee, J. C. 2000, ApJ, 545, L135

Schulz, N. S., Canizares, C., Huenemoerder, D., Kastner, J. H., Taylor, S. C., & Bergstrom, E. J. 2001, ApJ, 549, 441

Schulz, N. S., Canizares, C., Huenemoerder, D., & Tibbets, K. 2003, ApJ, 595, 365

Siess, L., Dufour, E., & Forestini, M. 2000, A&A, 358, 593

Simon, M., Close, L. M., & Beck, T. L. 1999, AJ, 117, 1375

Townsley, L. K., Broos, P. S., Nousek, J. A., & Garmire, G. P. 2002, Nuclear Instruments and Methods in Physics Research A, 486, 751

Townsley, L. K., Feigelson, E. D., Montmerle, T., Broos, P. S., Chu, Y., & Garmire, G. P. 2003, ApJ, 593, 874

Vuong, M. H., Montmerle, T., Grosso, N., Feigelson, E. D., Verstraete, L., & Ozawa, H. 2003, A&A, 408, 581

Weisskopf, M. C., Brinkman, B., Canizares, C., Garmire, G., Murray, S., & Van Speybroeck, L. P. 2001, PASP, 114, 1

Yamauchi, S., Koyama, K., Sakano, M., Okada, K. 1996, PASJ, 48, 719

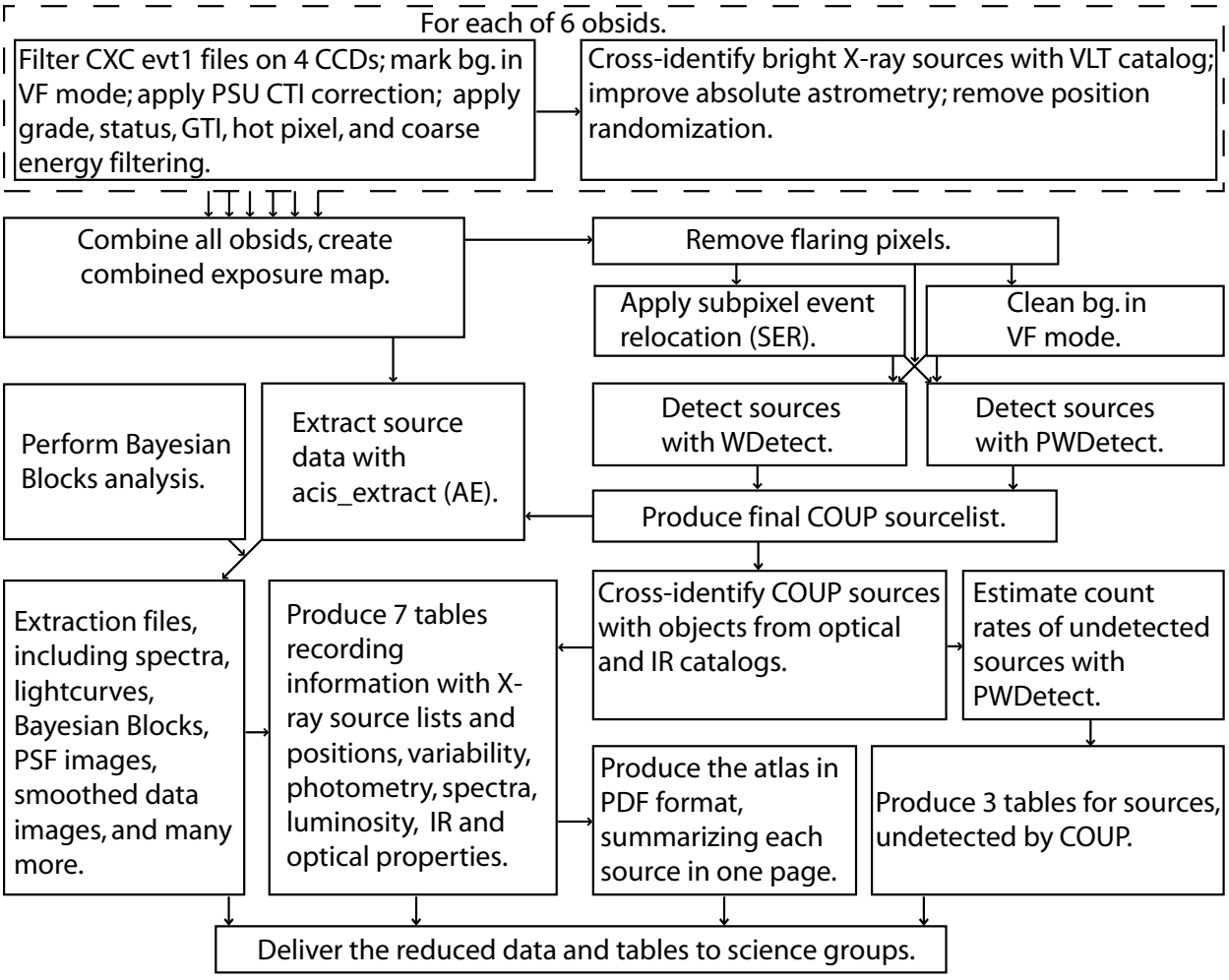


Fig. 1.— Diagram of the COUP data reduction and catalog procedure.

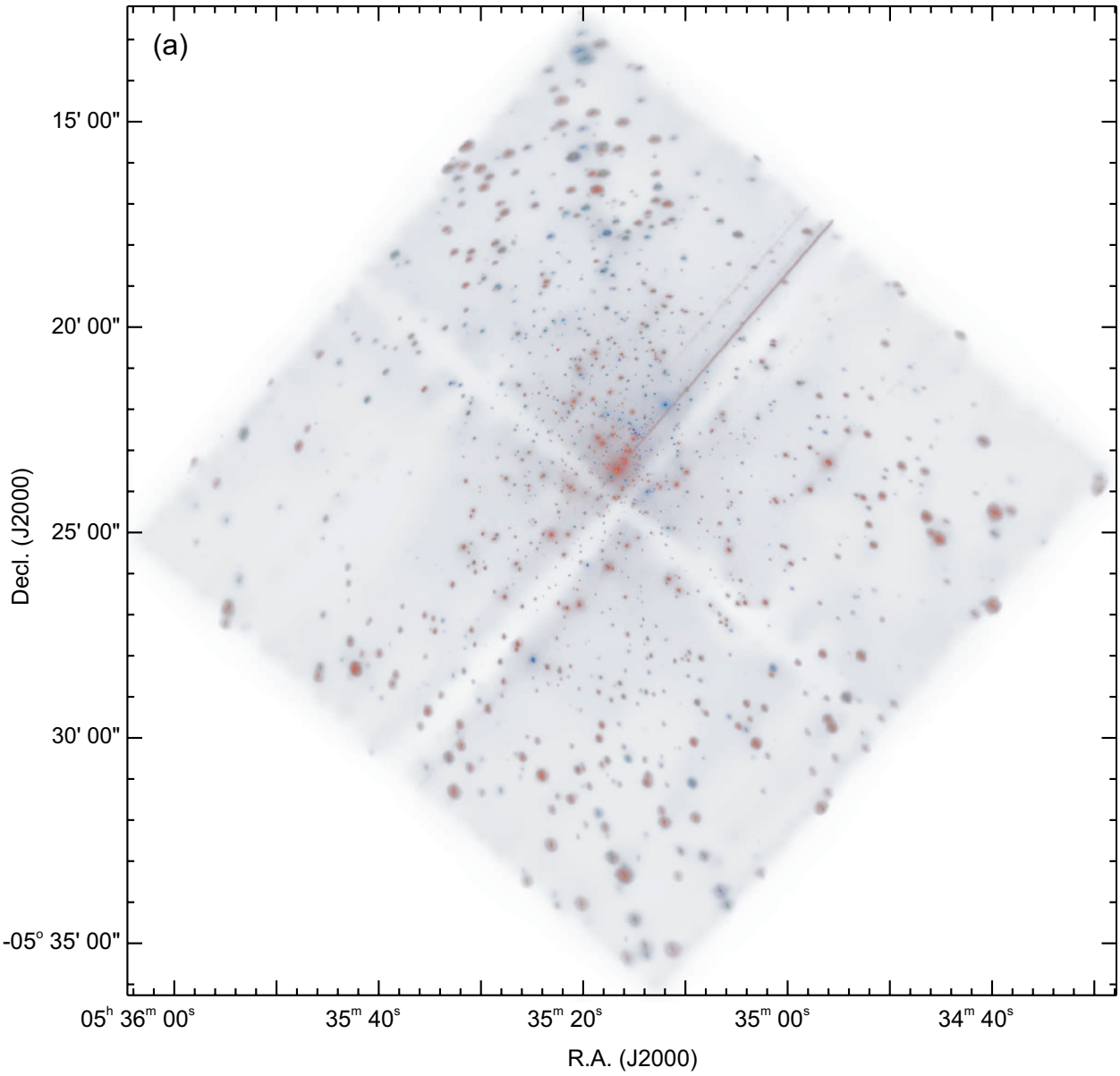


Fig. 2.— The COUP ACIS-I image: (a) the full ACIS-I field shown with 1″ pixels; and (b) the central region ($4' \times 4'$) shown with 0.25″ pixels. The image is shown after adaptive smoothing. The energy of each pixel is coded in color so that soft ($0.5 - 1.7$ keV) (unabsorbed) sources appear red while hard ($2.8 - 8.0$ keV), often absorbed, sources appear blue. Green indicates moderately absorbed sources with typical energies of $1.7 - 2.8$ keV. Brightness is scaled to the logarithm of the photon number in the displayed pixel. The color model depicts zero flux as white. Images are not corrected for the exposure map and thus show gaps between the four CCD chips.

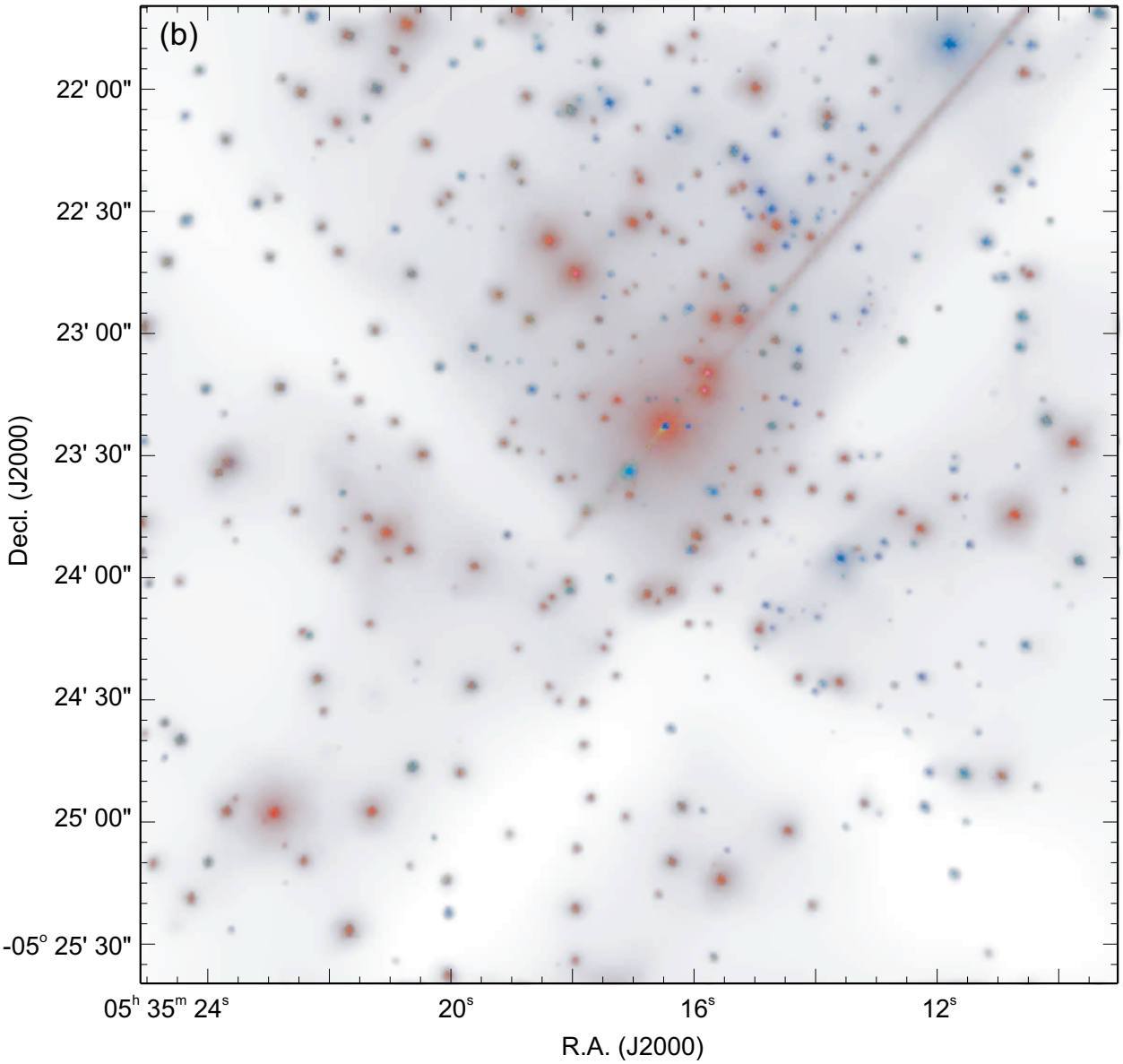
(b)
22' 00"
22' 30"
23' 00"
23' 30"
24' 00"
24' 30"
25' 00"
-05° 25' 30"
Decl. (J2000)
05h 35m 24s
20s
16s
12s
R.A. (J2000)

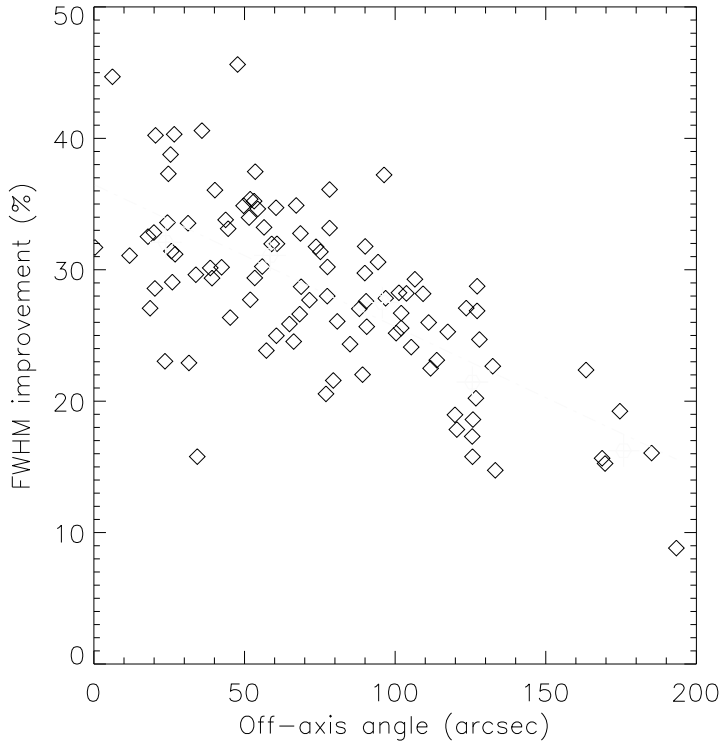


Fig. 3.— Improvement in the full width half-maximum (FWHM) width of the point spread function of 100 COUP sources due to application of the subpixel repositioning (SER) procedure.

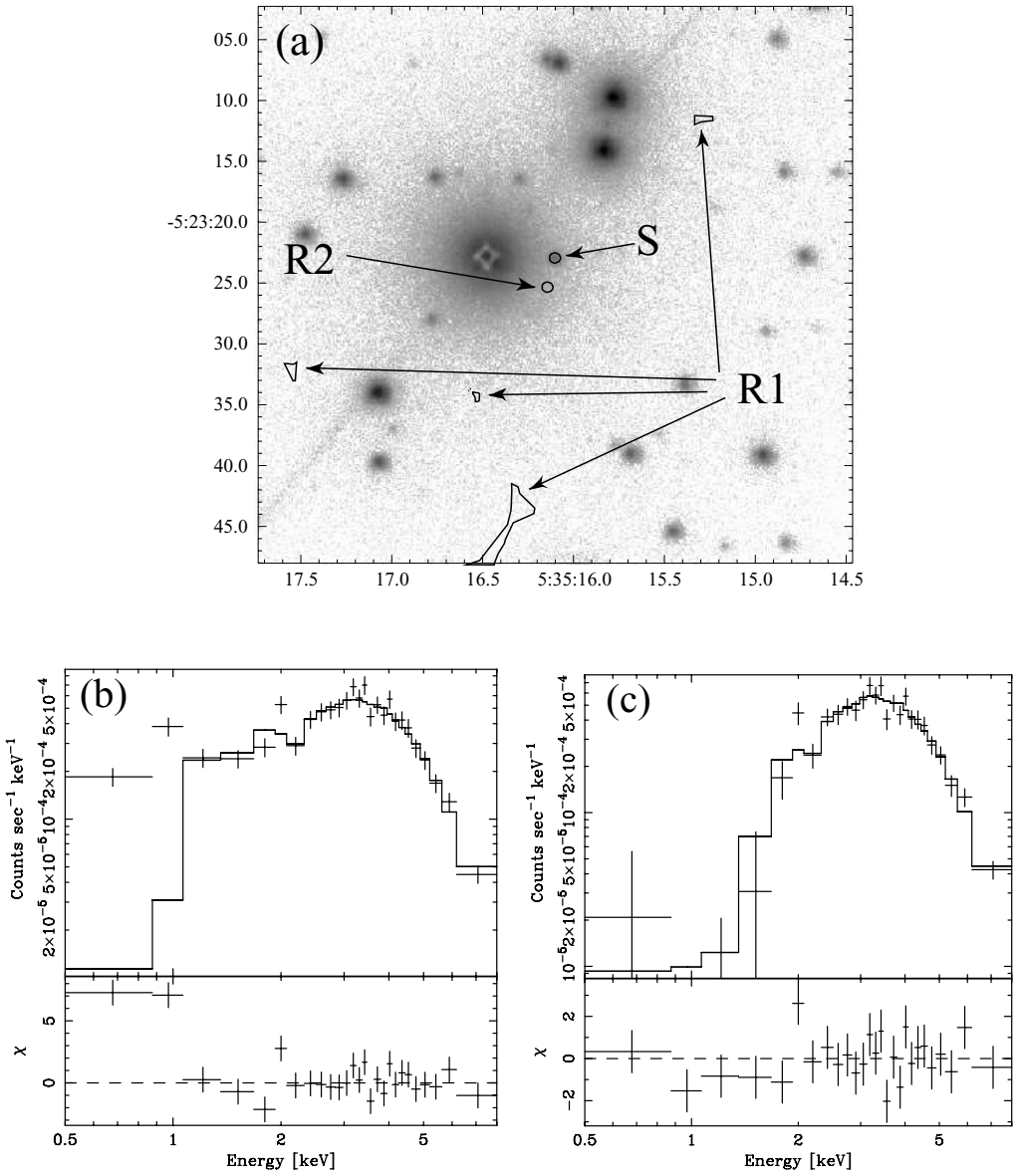


Fig. 4.— (a) Closeup view of the neighborhood of the sample source #780, located in a region of highly non-uniform background. $R_1$ marks the automatically extracted background region, $R_2$ is the manually improved local background, and S indicates the source extraction region. (Bottom) Spectra obtained through the subtraction of the automatically extracted background (b), and improved manually chosen background (c).

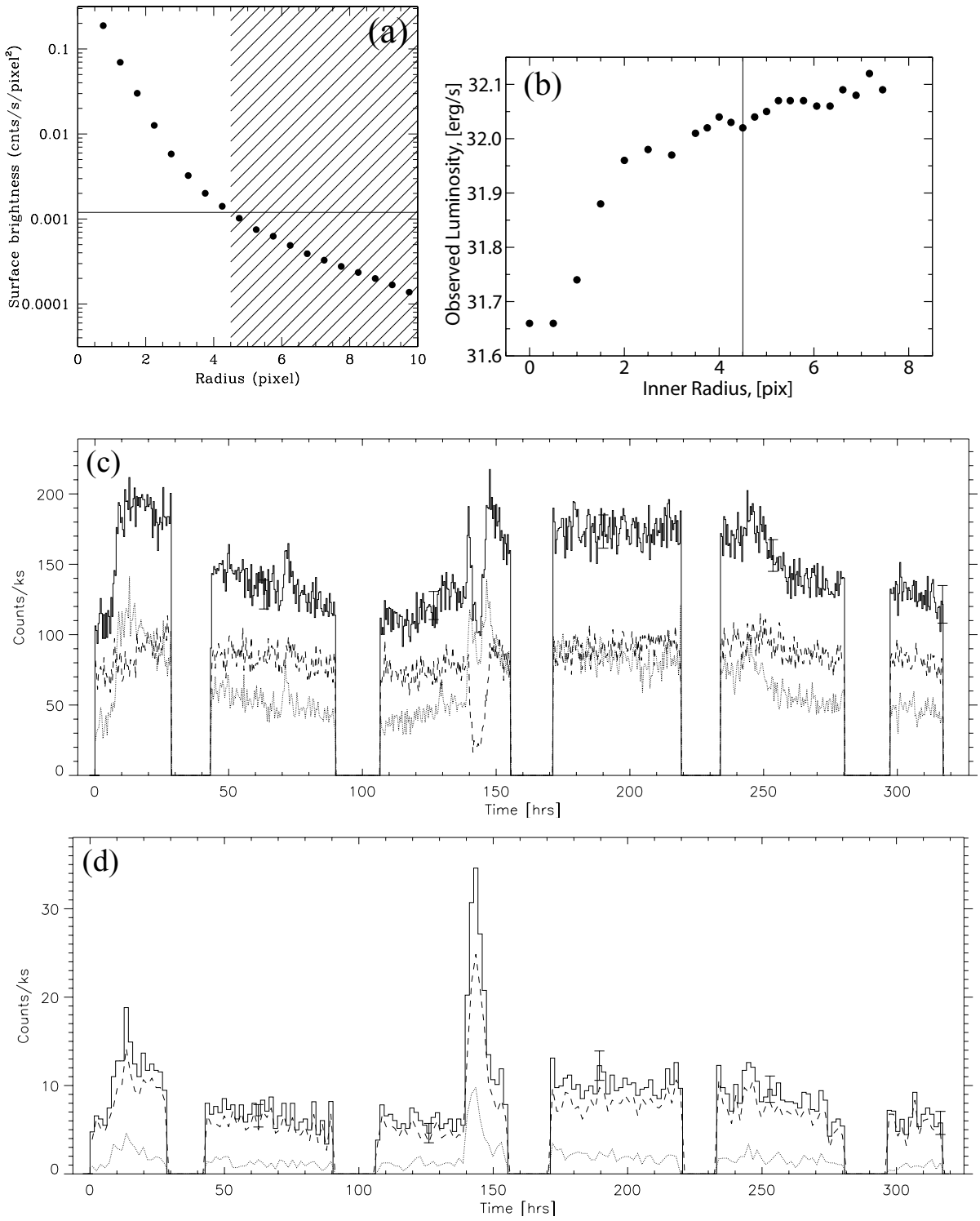


Fig. 5.— Study of the heavily piled-up COUP source #932: (a) the radial surface brightness profile of the piled-up events; (b) the inferred source luminosity as a function $r_{in}$ in our annular extraction technique for a series of excluded core sizes (the solid line marks the $\sim 2\%$ pile-up fraction); (c) lightcurve extracted from the usual extraction region including pile-up; and (d) lightcurve from the optimal annular extraction region. In the lightcurves, the solid line indicates the total energy band ($0.5-8$ keV), dashed line indicates the soft band ($0.5-2.0$ keV), and dotted line indicates the hard band ($2.0-8.0$ keV). Note that panel (c) shows a spurious dip while panel (d) shows the correct

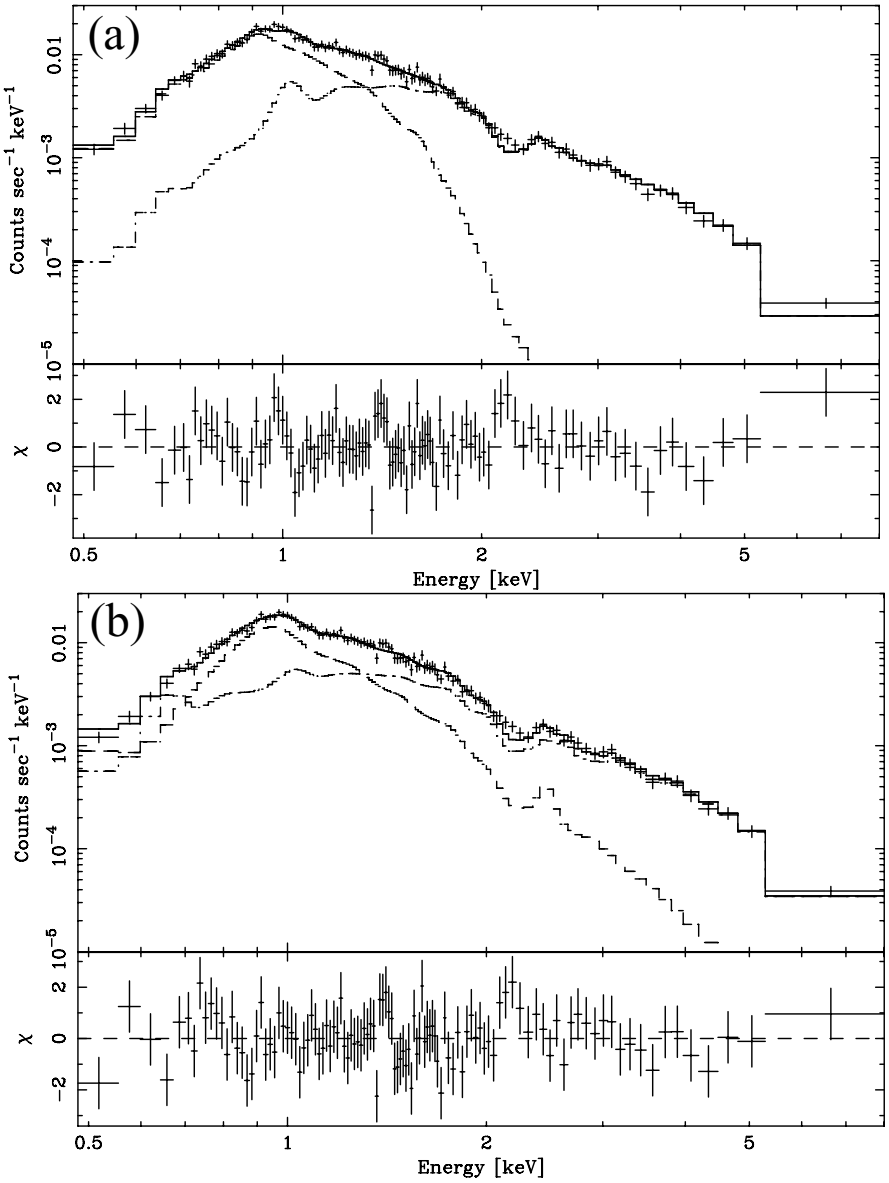


Fig. 6.— Spectrum of COUP source #567 exemplifying a common ambiguity in spectral fitting. Panel (a) presents a fit with $kT_1 \approx 0.2$ keV, $kT_2 \approx 1.7$ keV, $\log N_H \approx 21.8$ cm$^{-2}$, $\log L_{t,c} \approx 31.6$ erg/s with a reduced $\chi^2 \approx 1.3$. Panel (b) presents another fit (which appears in Table 6) with $kT_1 \approx 0.8$ keV, $kT_2 \approx 3.1$ keV, $\log N_H \approx 21.3$ cm$^{-2}$, $\log L_{t,c} \approx 30.6$ erg/s, and a reduced $\chi^2 \approx 1.4$. Note the 10-fold difference in inferred unabsorbed luminosity in the total $0.5 - 8$ keV band.

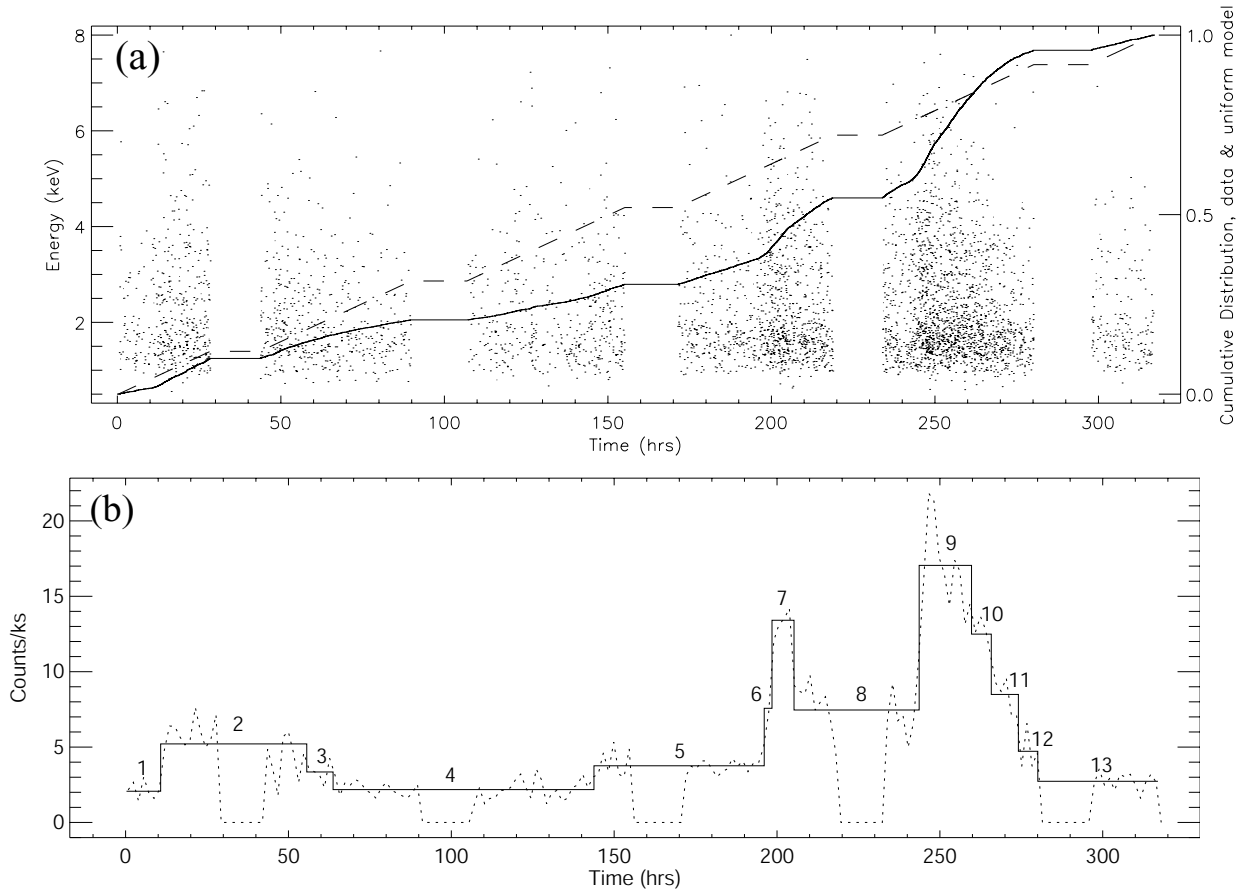


Fig. 7.— Variability analysis of COUP source #645. (a) Arrival times as a function of energy in the total $(0.5-8.0$ keV) energy band. The overplotted lines represent the cumulative distributions of the data (solid) and uniform model (dashed) used to compute KS variability test. (b) Bayesian Blocks segmentation (solid line) of the X-ray lightcurve (dotted line) in the total energy band.

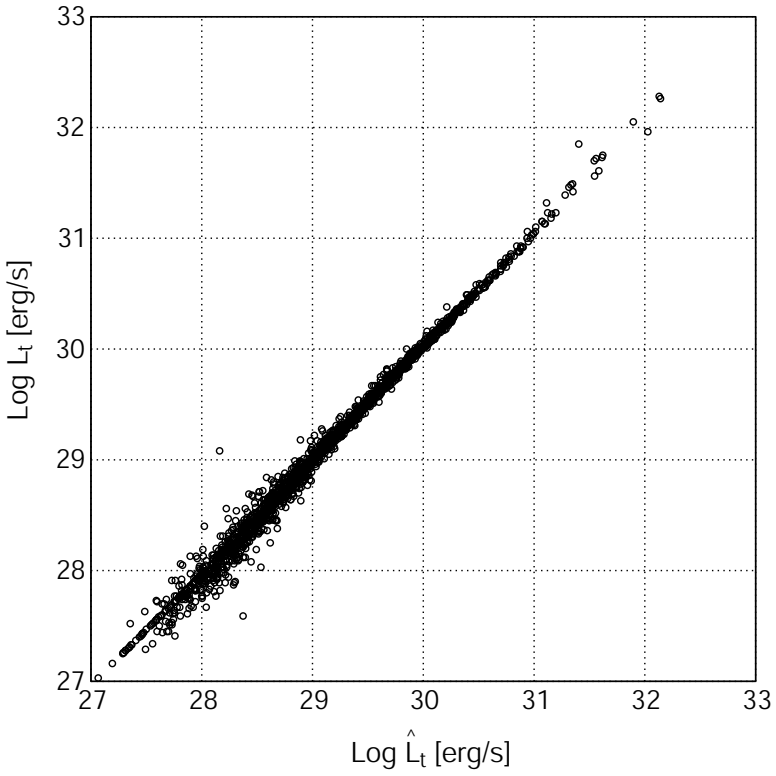


Fig. 8.— Scatter plot of total band luminosities $L_t$ inferred from *XSPEC* spectral fitting with the approximate luminosity $\hat{L}_t$ derived from photometric data.

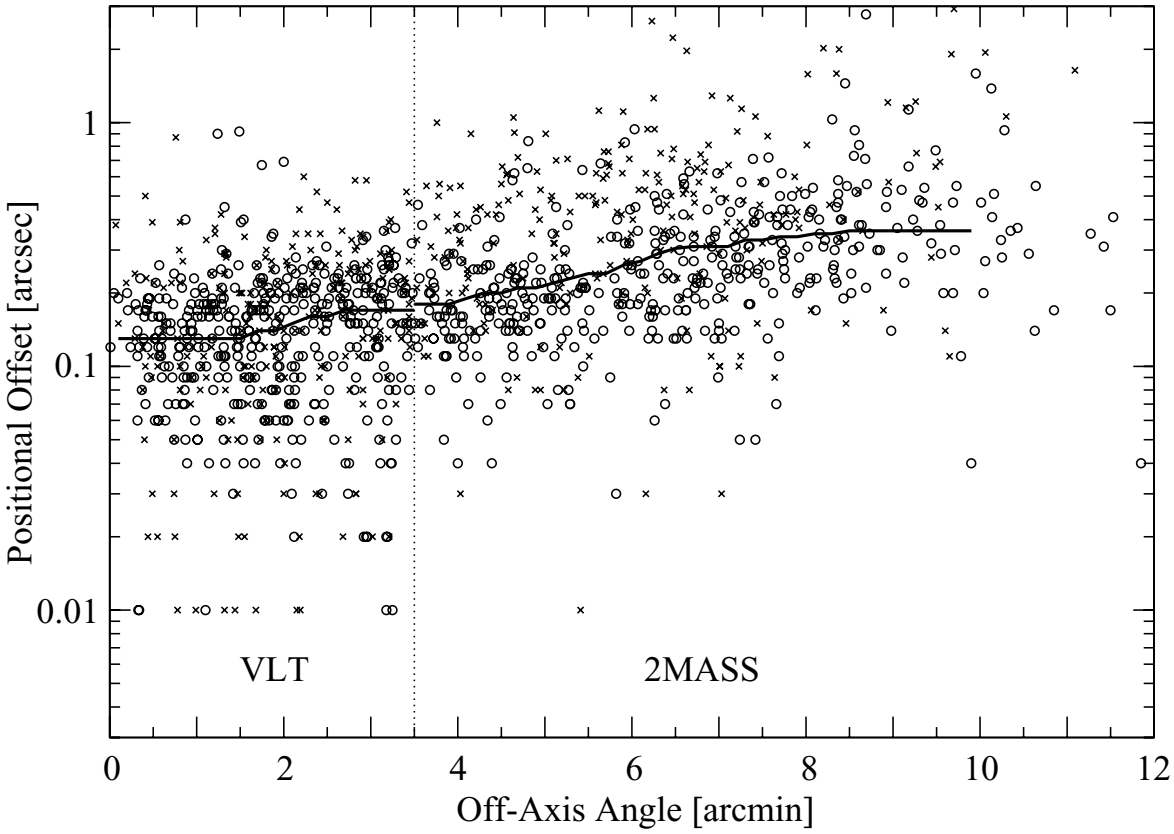


Fig. 9.— Separations between COUP X-ray sources and IR counterparts. For each individual source symbols present separations between COUP and VLT catalog within the inner $< 3.5'$ region, and COUP and 2MASS catalog within the outer $> 3.5'$ region. X indicate weak X-ray sources with $< 200$ counts, circles indicate bright X-ray sources with $\geq 200$ counts. Solid lines present the running medians of separations.

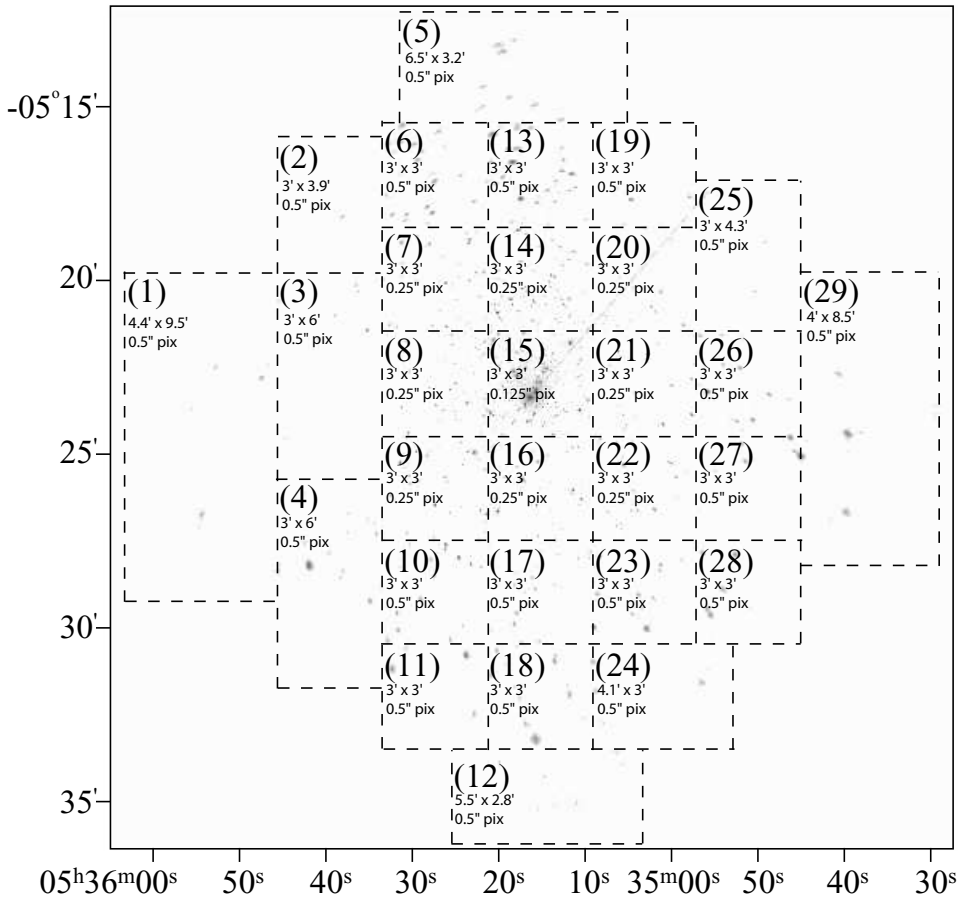


Fig. 10.— Guide to the expanded views of the merged COUP ACIS-I data.

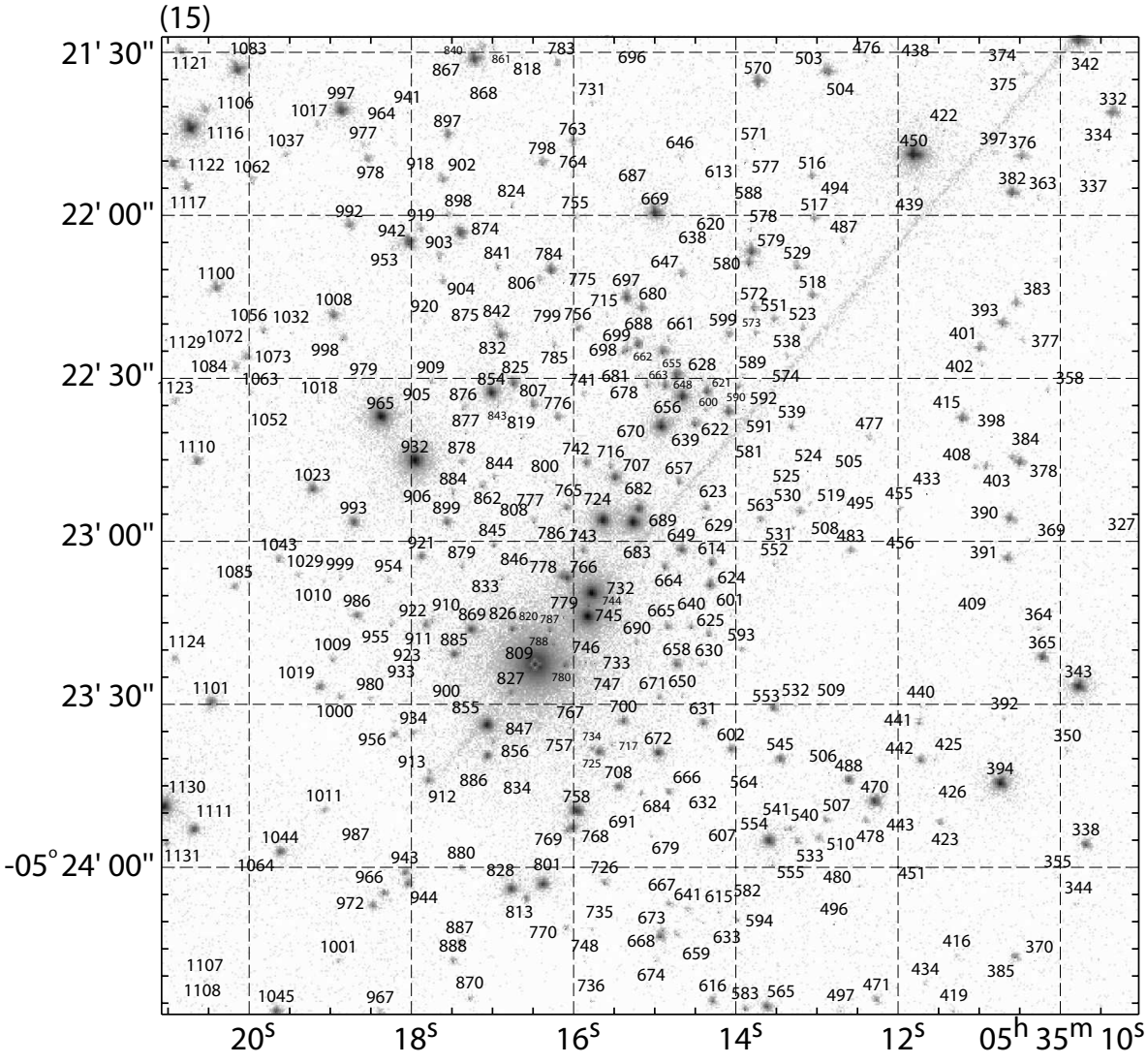


Fig. 11.— Expanded views of the merged COUP ACIS-I data with sources indicated. Panel numbers are indicated in parentheses in the upper left corner of each panel and refer back to Figure 10.

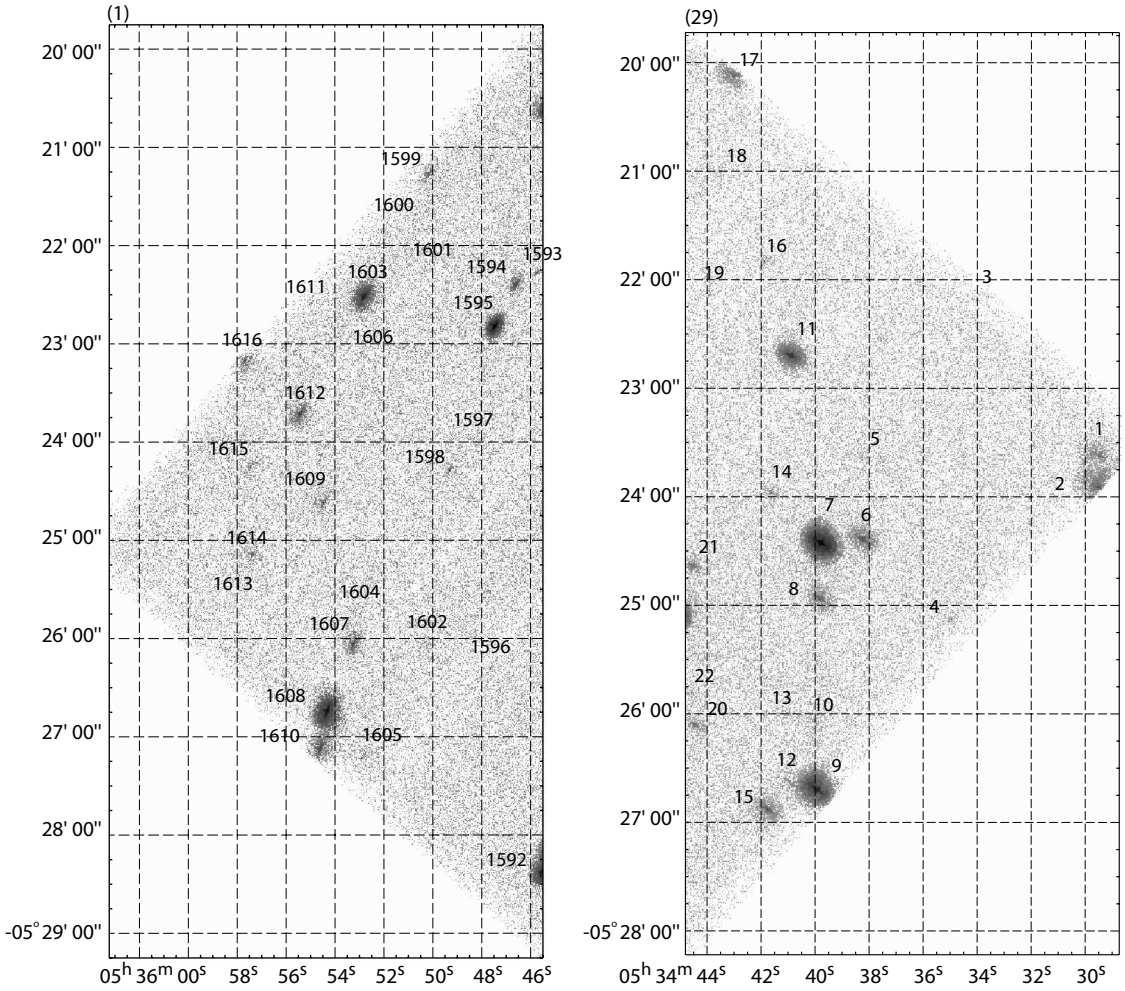
(1)
20' 00"
21' 00"
22' 00"
23' 00"
24' 00"
25' 00"
26' 00"
27' 00"
28' 00"
-05° 29' 00"
05h 36m 00s 58s 56s 54s 52s 50s 48s 46s
1599
1600
1601
1593
1594
1603
1611
1595
1616
1606
1612
1597
1615
1598
1609
1614
1613
1604
1607
1602
1596
1608
1610
1605
1592
(29)
20' 00"
21' 00"
22' 00"
23' 00"
24' 00"
25' 00"
26' 00"
27' 00"
-05° 28' 00"
05h 34m 44s 42s 40s 38s 36s 34s 32s 30s
17
18
16
19
3
11
1
5
14
2
7
6
21
8
4
22
20
13
10
12
9
15

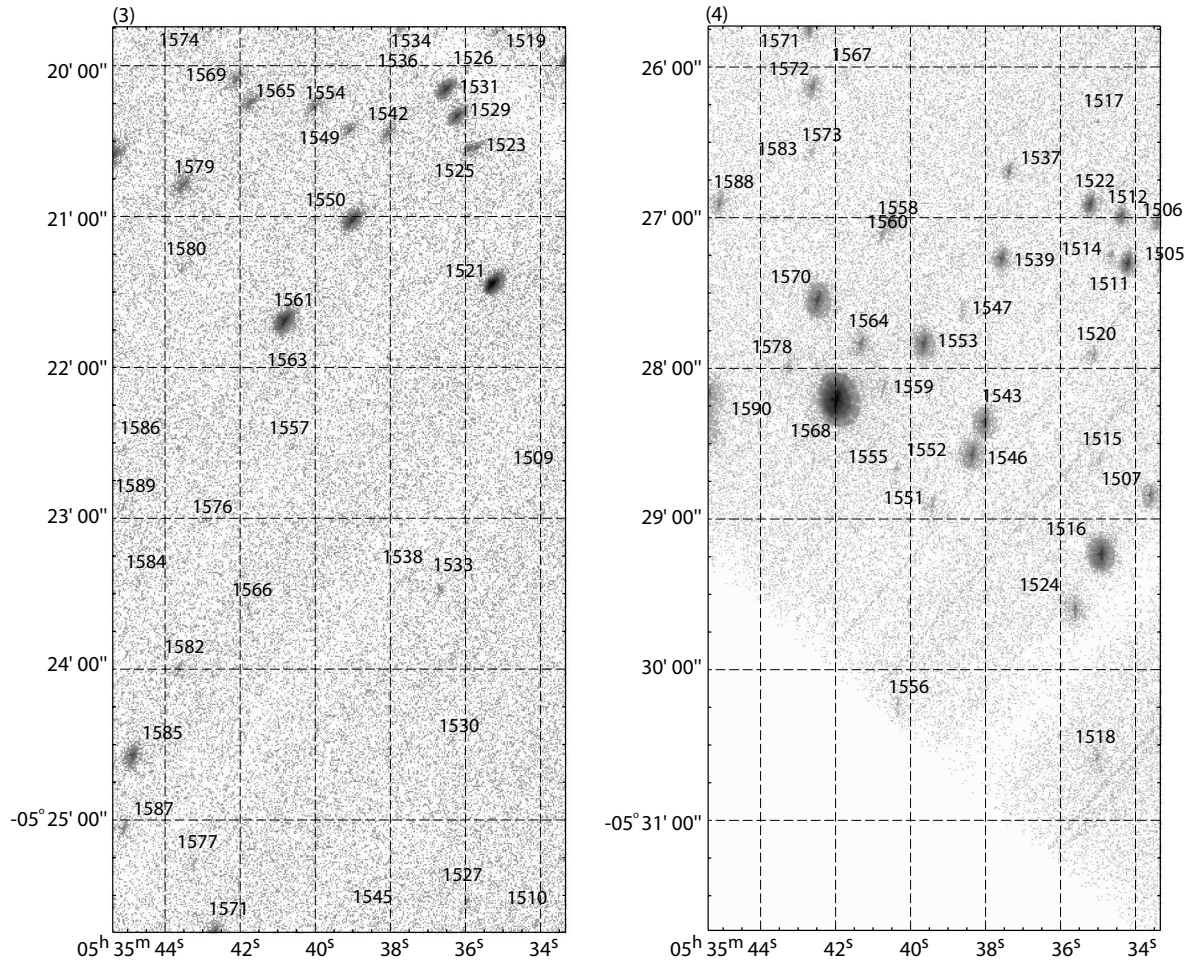
(3)
1574
1534
1519
1536
1526
1569
1531
1565
1554
1529
1542
1549
1523
1579
1525
1550
1580
1521
1561
1563
1586
1557
1509
1589
1576
1584
1538
1533
1566
1582
1530
1585
1587
1577
1527
1545
1510
1571
20' 00"
21' 00"
22' 00"
23' 00"
24' 00"
-05° 25' 00"
05h 35m 44s
42s
40s
38s
36s
34s
(4)
1571
1567
1572
1517
1573
1583
1537
1588
1522
1512
1558
1506
1560
1514
1539
1505
1570
1511
1547
1564
1520
1578
1553
1559
1543
1590
1568
1515
1555
1552
1546
1507
1551
1516
1524
1556
1518
26' 00"
27' 00"
28' 00"
29' 00"
30' 00"
-05° 31' 00"
05h 35m 44s
42s
40s
38s
36s
34s

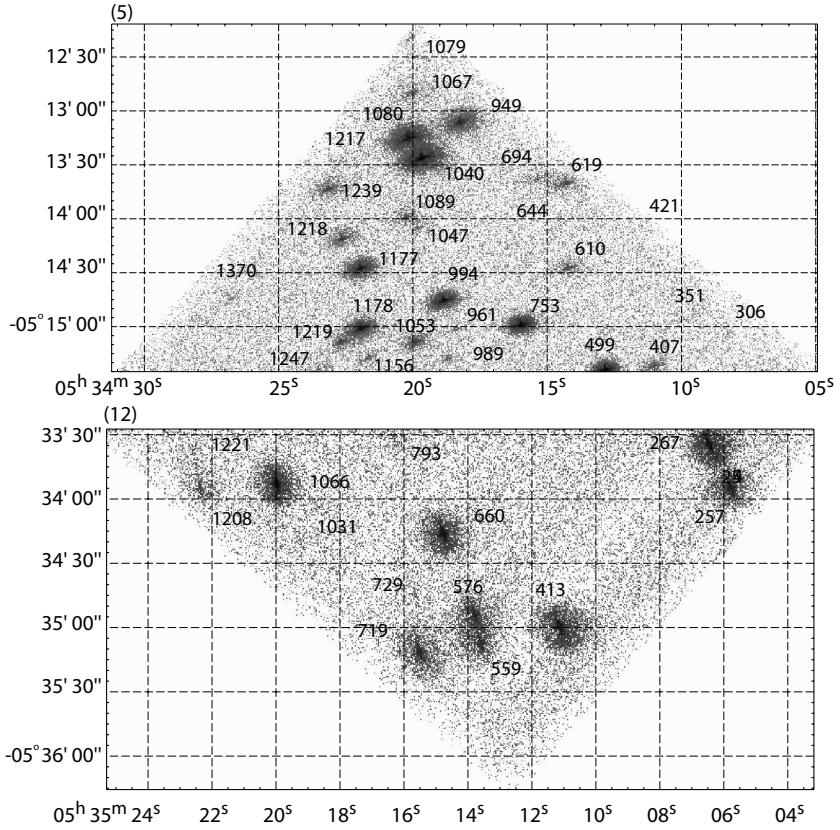
(5)
12' 30"
13' 00"
13' 30"
14' 00"
14' 30"
-05° 15' 00"
05h 34m 30s
25s
20s
15s
10s
05s
1079
1067
1080
949
1217
694
619
1040
1239
1089
644
421
1218
1047
610
1177
1370
994
351
1178
753
306
961
1219
1053
499
407
1247
989
1156
(12)
33' 30"
34' 00"
34' 30"
35' 00"
35' 30"
-05° 36' 00"
05h 35m 24s
22s
20s
18s
16s
14s
12s
10s
08s
06s
04s
1221
793
267
1066
1208
1031
660
257
729
576
413
719
559

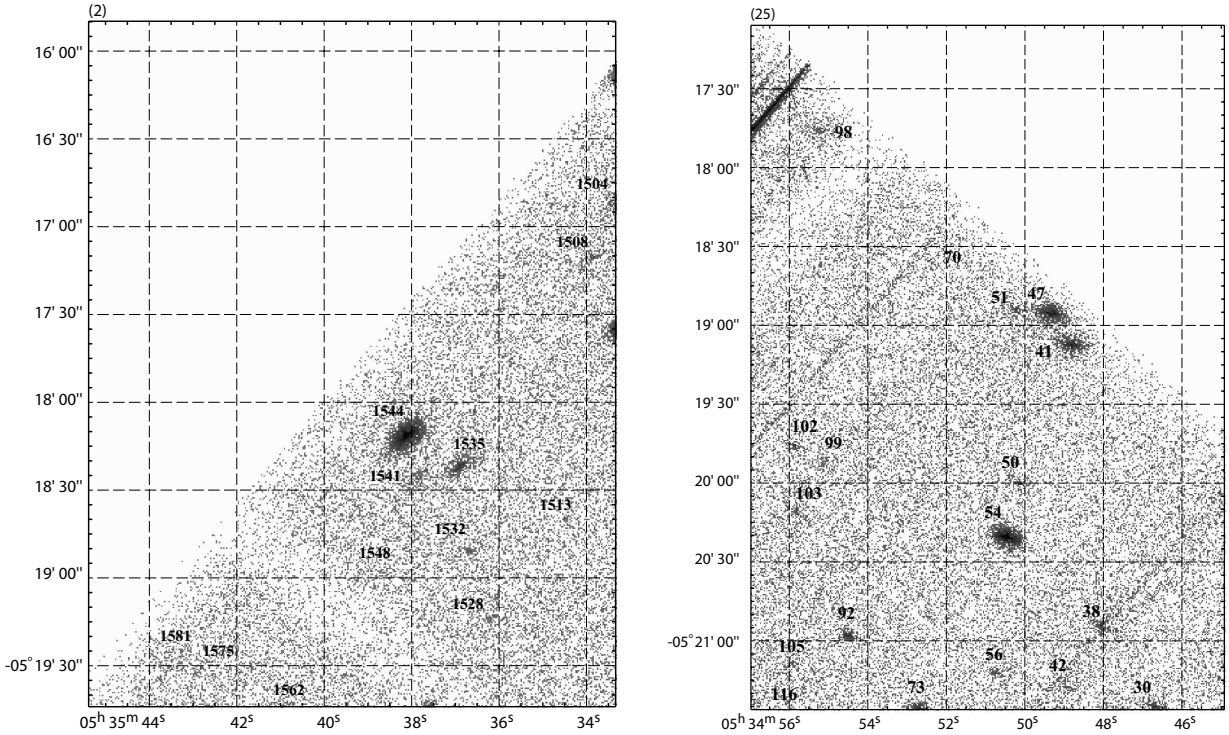
(2)
16' 00"
16' 30"
17' 00"
17' 30"
18' 00"
18' 30"
19' 00"
-05° 19' 30"
05h 35m 44s
42s
40s
38s
36s
34s
1504
1508
1544
1535
1541
1513
1532
1548
1528
1581
1575
1562
(25)
17' 30"
18' 00"
18' 30"
19' 00"
19' 30"
20' 00"
20' 30"
-05° 21' 00"
05h 34m 56s
54s
52s
50s
48s
46s
98
70
51
47
41
102
99
50
103
54
92
38
105
56
42
116
73
30

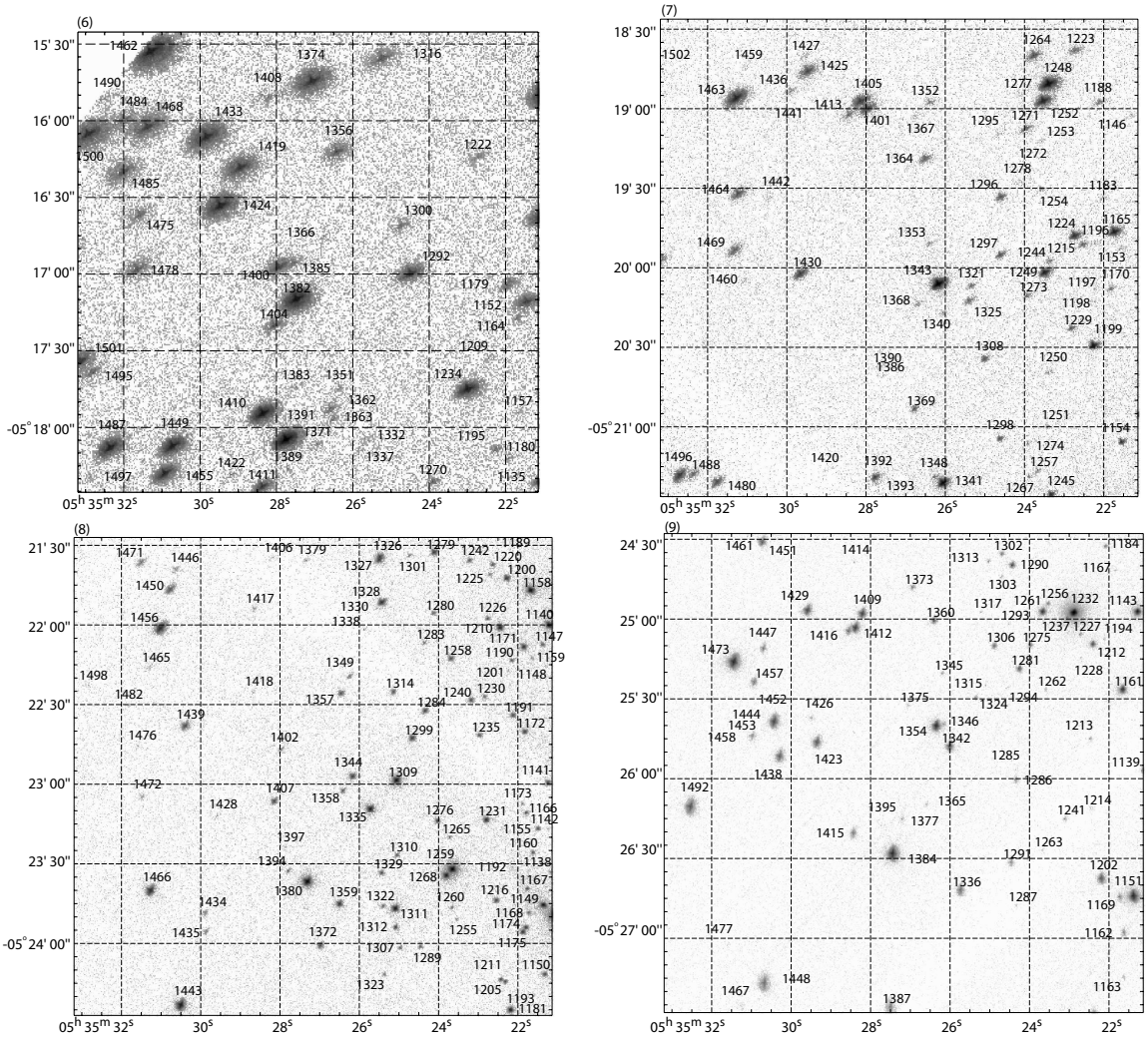
(6)
(7)
(8)
(9)
15' 30"
16' 00"
16' 30"
17' 00"
17' 30"
-05° 18' 00"
18' 30"
19' 00"
19' 30"
20' 00"
20' 30"
-05° 21' 00"
21' 30"
22' 00"
22' 30"
23' 00"
23' 30"
-05° 24' 00"
24' 30"
25' 00"
25' 30"
26' 00"
26' 30"
-05° 27' 00"
05h 35m 32s
30s
28s
26s
24s
22s

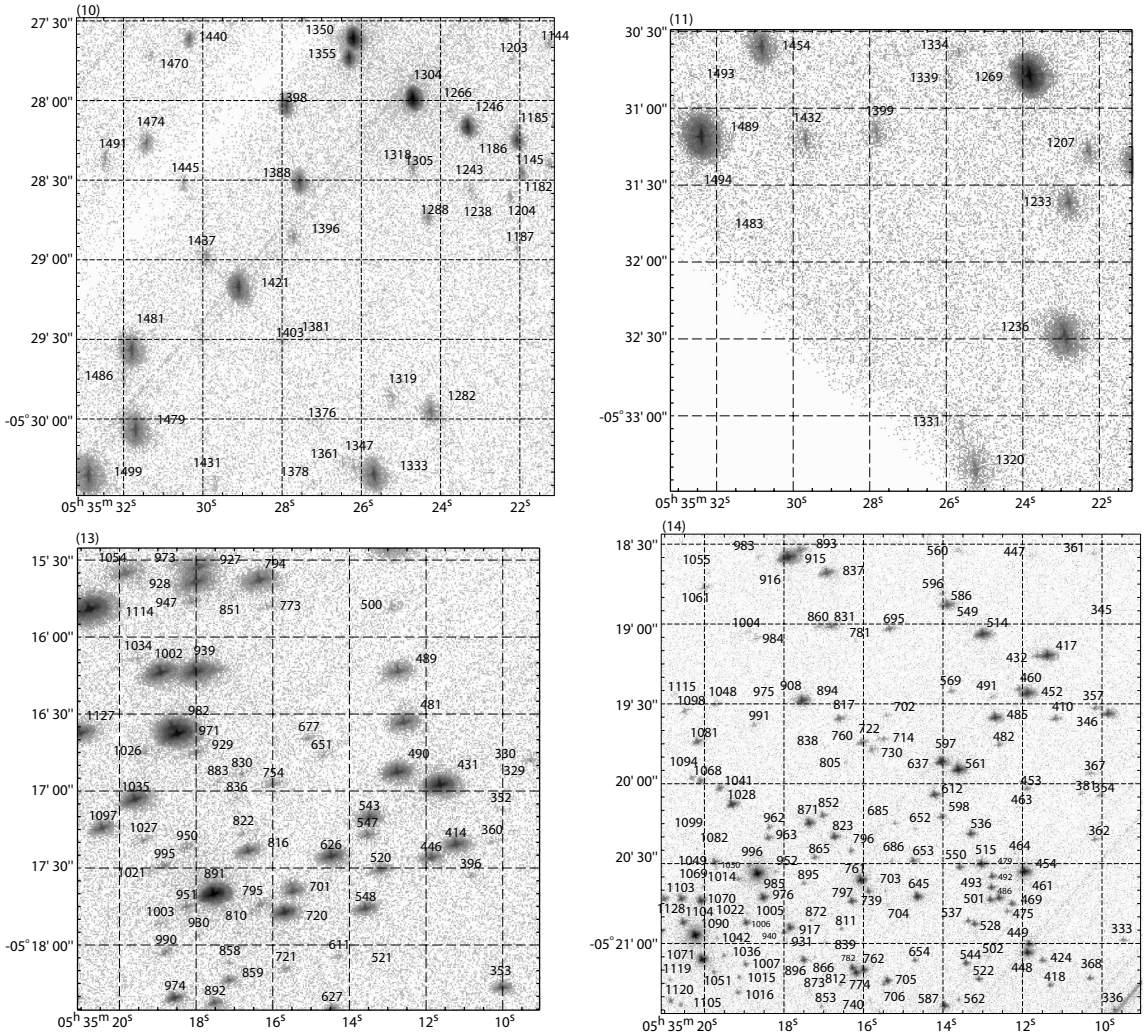
(10)
(11)
(13)
(14)

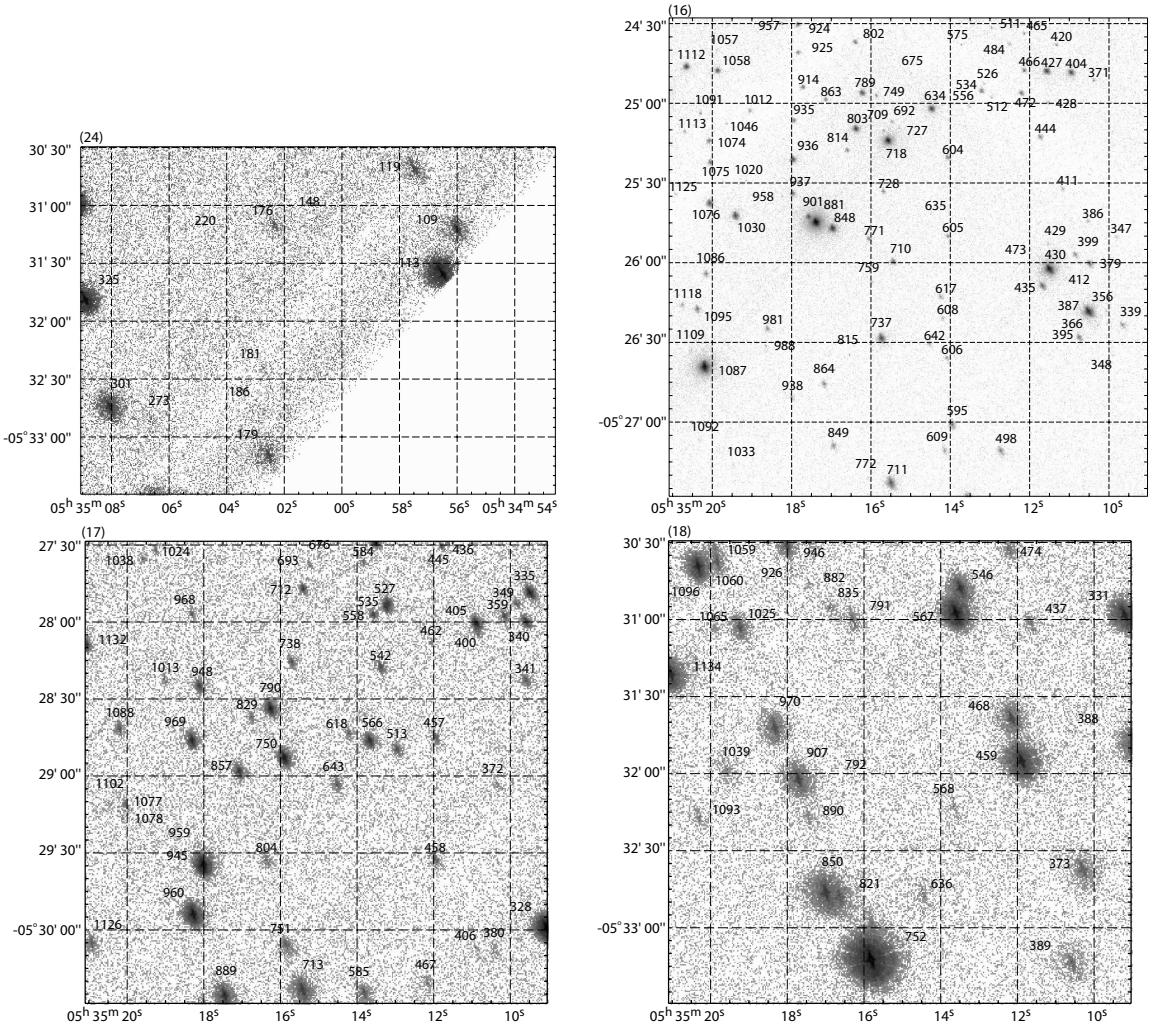
(24)
(16)
(17)
(18)

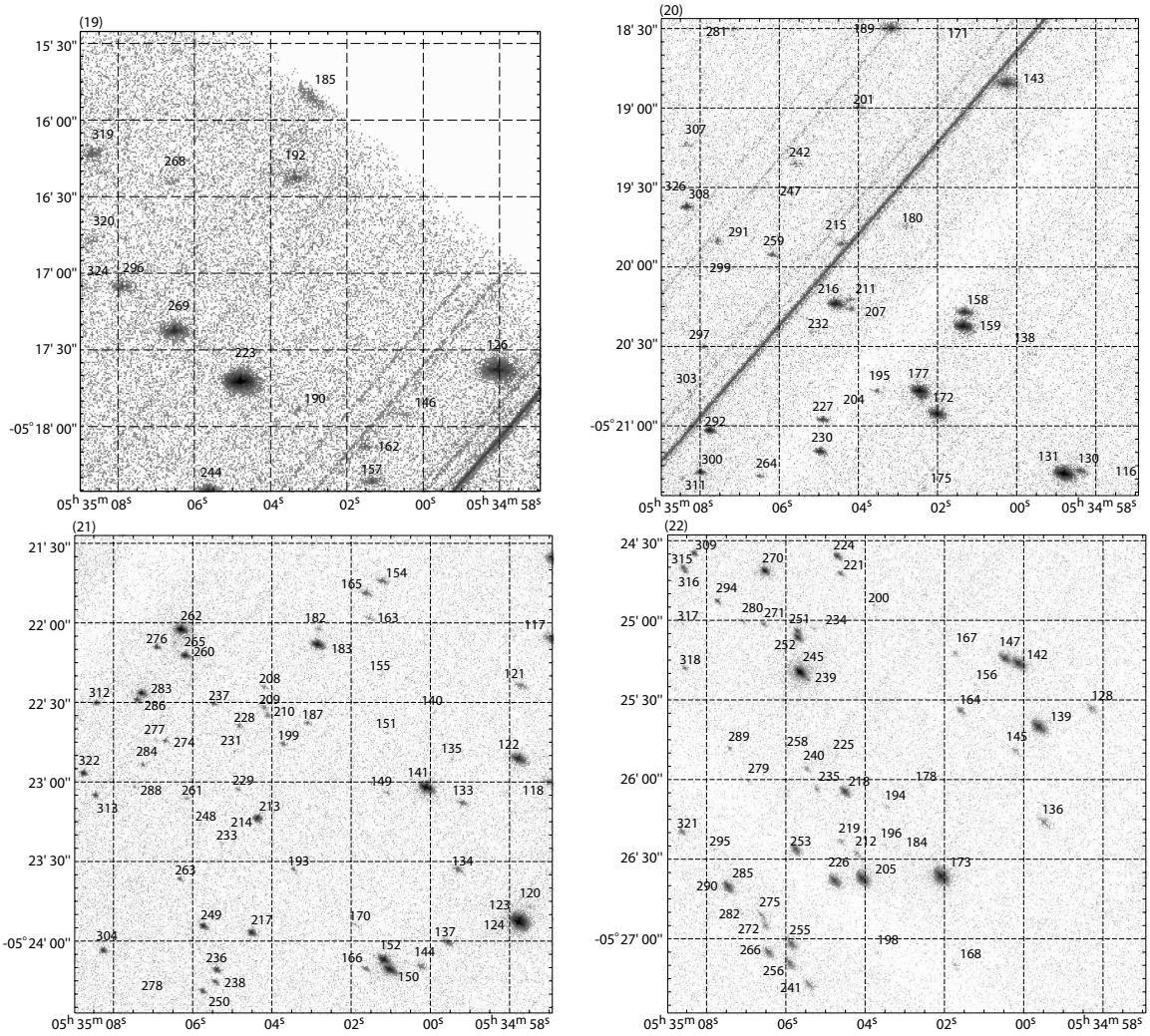
(19)
(20)
(21)
(22)
15' 30"
16' 00"
16' 30"
17' 00"
17' 30"
-05° 18' 00"
18' 30"
19' 00"
19' 30"
20' 00"
20' 30"
-05° 21' 00"
21' 30"
22' 00"
22' 30"
23' 00"
23' 30"
-05° 24' 00"
24' 30"
25' 00"
25' 30"
26' 00"
26' 30"
-05° 27' 00"
05h 35m 08s
06s
04s
02s
00s
05h 34m 58s

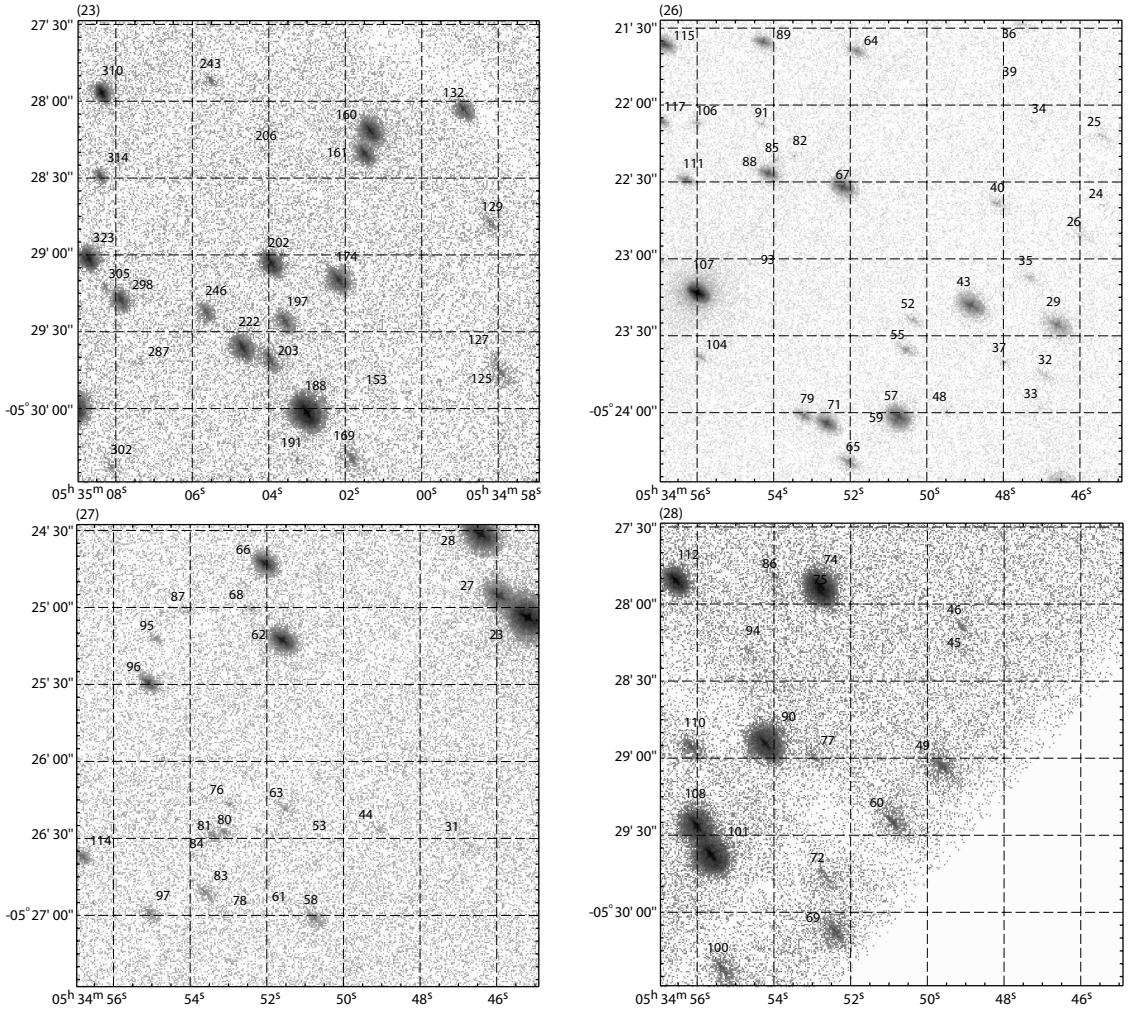
(23)
27' 30''
28' 00''
28' 30''
29' 00''
29' 30''
-05° 30' 00''
05h 35m 08s
06s
04s
02s
00s
05h 34m 58s
310
243
132
160
206
161
314
129
323
202
174
305
298
246
197
222
287
203
127
188
153
125
191
169
302
(26)
21' 30''
22' 00''
22' 30''
23' 00''
23' 30''
-05° 24' 00''
05h 34m 56s
54s
52s
50s
48s
46s
115
89
64
86
39
117
106
91
34
25
85
82
111
88
67
40
24
26
107
93
35
43
52
29
55
104
37
32
79
71
57
48
33
59
65
(27)
24' 30''
25' 00''
25' 30''
26' 00''
26' 30''
-05° 27' 00''
05h 34m 56s
54s
52s
50s
48s
46s
66
28
87
68
27
95
62
23
96
76
63
81
80
53
44
31
114
84
83
97
78
61
58
(28)
27' 30''
28' 00''
28' 30''
29' 00''
29' 30''
-05° 30' 00''
05h 34m 56s
54s
52s
50s
48s
46s
112
86
74
75
46
94
45
110
90
77
49
108
60
101
72
69
100

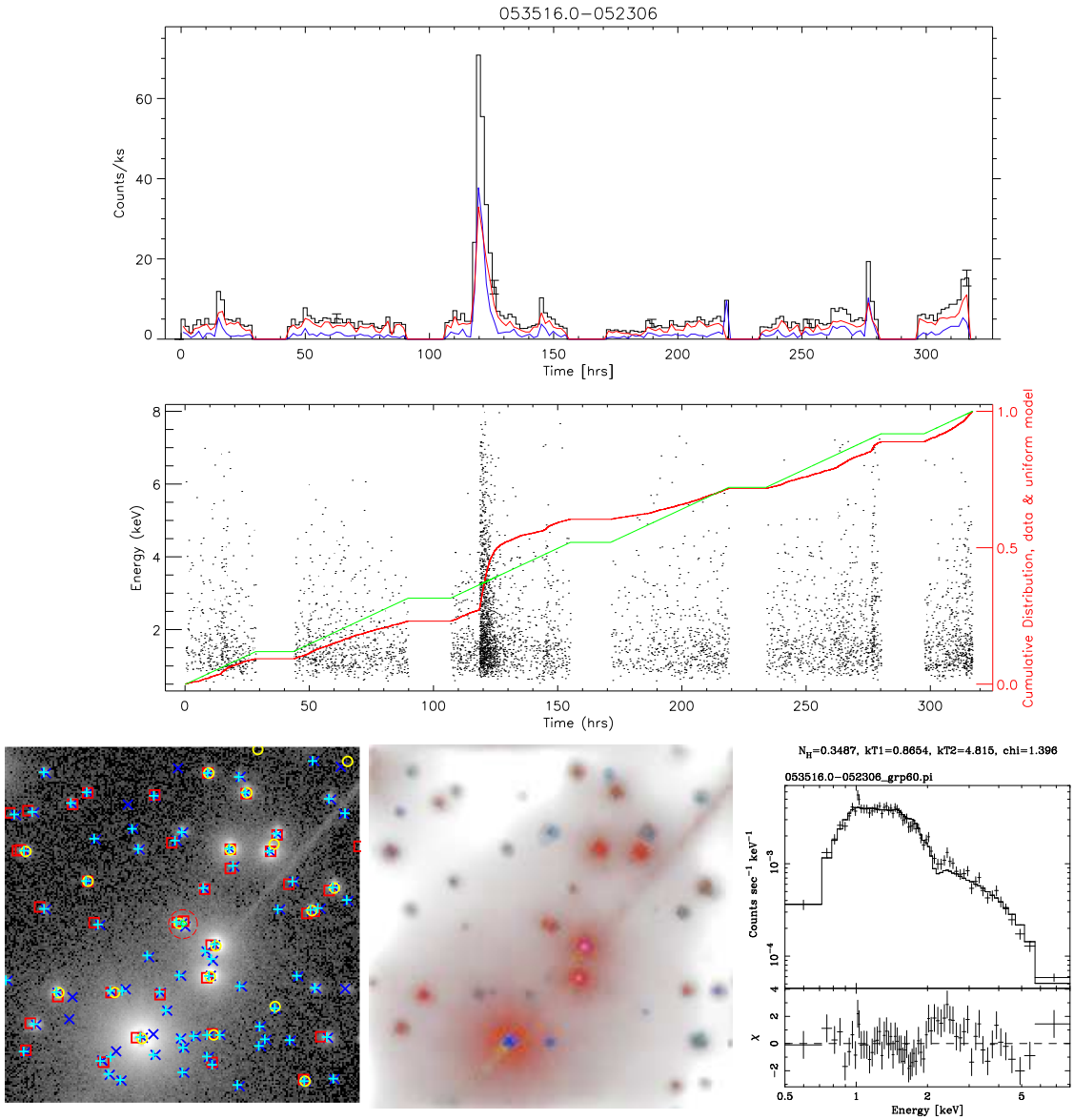


| | | | | | | | | | | | |
|---|---|---|---|---|---|---|---|---|---|---|---|
| Seq | 766 | CXOONCJ | 053516.0-052306 | RAdeg | 83.817009 | DEdeg | -5.385267 | Offaxis | 0.60 | ACIS# | 519 |
| HRC# | 340 | JHK-Src | 565 | JHK-Off | 0.09 | J | 9.74 | H | 8.37 | Ks | 7.35 |
| Ph-Flg | 555 | L-RfFlg | M | L-Src | 460A | L | 5.50 | H97-Src | 1863b | H97-Off | 0.43 |
| H97-V | — | H97-I | 11.00 | SpTy | — | Av | — | Mass | — | Age | — |
| NetCts | 5091 | BkgCts | 7 | PSFFrac | 0.39 | ExpTime | 832.9 | MedEn | 1.58 | HR1 | -0.32 |
| ChipGap | — | logPbKS | -4.0 | BB# | 20 | BBMin | 1.76 | BBMax | 109.45 | logNH | 21.54 |
| kT1 | 0.87 | kT2 | 4.82 | logEM1 | 52.83 | logEM2 | 53.52 | chi2 | 1.40 | dof | 61 |
| logLs | 30.07 | logLh | 30.41 | logLh-c | 30.42 | logLt | 30.57 | logLt-c | 30.71 | | |
| Comments: | | | | | | | | | | | |

Fig. 12.— Sample page from the COUP source atlas.

Table 1. COUP Observations

| ObsID | Start Time | Exposure (ks) | Right Ascension (degrees J2000) | Declination | Roll Angle degrees |
|---|---|---|---|---|---|
| 4395 | 2003 Jan 08 20:58:18.8 | 99.9 | 83.8210052 | -5.394400 | 310.90882 |
| 3744 | 2003 Jan 10 16:17:38.7 | 164.2 | 83.8210086 | -5.394406 | 310.90882 |
| 4373 | 2003 Jan 13 07:34:43.5 | 171.5 | 83.8210098 | -5.394403 | 310.90882 |
| 4374 | 2003 Jan 16 00:00:37.4 | 168.9 | 83.8210079 | -5.394404 | 310.90882 |
| 4396 | 2003 Jan 18 14:34:48.3 | 164.5 | 83.8210094 | -5.394403 | 310.90882 |
| 3498 | 2003 Jan 21 06:10:27.7 | 69.1 | 83.8210025 | -5.394402 | 310.90882 |

Note. — ObsID values are from the *Chandra* Observation Catalog. Start Times are in UT. Exposure times are the sum of Good Time Intervals (GTIs) for the CCD at the telescope aim point (CCD3) minus 1.3% to account for CCD readouts. The aimpoints and roll angles are obtained from the satellite aspect solution before astrometric correction was applied.

Table 2. COUP X-ray Source Locations

| Source | | Position | | | | Detection | | | | | Previous | |
|---|---|---|---|---|---|---|---|---|---|---|---|---|
| Seq | CXOONCJ | R.A. | Decl. | Err | $\theta$ | Flag | Flag | Flag | Signif | Signif | ACIS | HRC |
| # | | (degrees J2000) | | $''$ | $'$ | 1 | 2 | 3 | A_E | PWD | # | # |
| (1) | (2) | (3) | (4) | (5) | (6) | (7) | (8) | (9) | (10) | (11) | (12) | (13) |
| 1 | 053429.4-052337 | 83.622730 | -5.393730 | 0.16 | 11.85 | 0d000x | 11 | 110 | 23.9 | 36.0 | ··· | ··· |
| 2 | 053429.5-052354 | 83.623040 | -5.398490 | 0.11 | 11.83 | 0d000x | 11 | 110 | 41.0 | 94.4 | ··· | 10 |
| 3 | 053433.9-052211 | 83.641473 | -5.369767 | 0.59 | 10.83 | 00000x | 10 | 100 | 0.6 | ··· | ··· | ··· |
| 4 | 053434.9-052507 | 83.645653 | -5.418817 | 0.38 | 10.58 | 00000x | 10 | 100 | 0.5 | ··· | ··· | ··· |
| 5 | 053438.2-052338 | 83.659339 | -5.393952 | 0.35 | 9.66 | 000000 | 11 | 110 | 4.0 | 7.0 | ··· | ··· |
| 6 | 053438.2-052423 | 83.659281 | -5.406534 | 0.09 | 9.69 | 0000w0 | 11 | 110 | 28.8 | 77.3 | 2 | ··· |
| 7 | 053439.7-052425 | 83.665798 | -5.407138 | 0.01 | 9.30 | 00p000 | 11 | 110 | 198.6 | 452.7 | 4 | 18 |
| 8 | 053439.8-052456 | 83.665915 | -5.415641 | 0.12 | 9.35 | 0000w0 | 11 | 110 | 24.3 | 54.9 | 3 | ··· |
| 9 | 053439.9-052642 | 83.666336 | -5.445000 | 0.04 | 9.73 | 0d000x | 11 | 110 | 123.3 | 239.6 | 6 | 20 |
| 10 | 053440.0-052604 | 83.666807 | -5.434478 | 0.30 | 9.52 | 0d0000 | 11 | 110 | 4.0 | 11.7 | ··· | ··· |
| 11 | 053440.8-052242 | 83.670374 | -5.378408 | 0.04 | 9.05 | 00000x | 11 | 110 | 72.7 | 160.8 | 9 | 21 |
| 12 | 053440.8-052639 | 83.670220 | -5.444250 | 0.18 | 9.49 | 0d000x | 10 | 002 | 15.4 | ··· | 7 | ··· |
| 13 | 053440.9-052559 | 83.670779 | -5.433305 | 0.33 | 9.27 | 0d0000 | 11 | 110 | 1.8 | 6.7 | 8 | ··· |
| 14 | 053441.6-052357 | 83.673450 | -5.399378 | 0.24 | 8.82 | 0000wx | 11 | 110 | 7.7 | 18.9 | ··· | ··· |
| 15 | 053441.7-052652 | 83.673936 | -5.448017 | 0.12 | 9.36 | 0d000x | 11 | 110 | 25.3 | 64.9 | 10 | ··· |

Note. — See §4.3 for description of the columns. The full table of 1616 COUP sources is available in the electronic edition of the Journal.

Table 3. Tentative COUP Sources

| CXOONCJ | R.A. (degrees J2000) | Decl. |
|---|---|---|
| 053503.8-051758 | 83.765885 | -5.299651 |
| 053503.9-052253 | 83.766622 | -5.381438 |
| 053504.0-052809 | 83.766730 | -5.469410 |
| 053504.5-051908 | 83.768862 | -5.318981 |
| 053505.7-052616 | 83.774150 | -5.437980 |
| 053508.6-052022 | 83.785996 | -5.339450 |
| 053508.8-052015 | 83.786847 | -5.337515 |
| 053509.8-052143 | 83.791170 | -5.362130 |
| 053510.4-052430 | 83.793640 | -5.408600 |
| 053510.7-051940 | 83.794591 | -5.327879 |
| 053512.8-052156 | 83.803440 | -5.365780 |
| 053513.2-052322 | 83.805251 | -5.389650 |
| 053513.5-052209 | 83.806492 | -5.369288 |
| 053515.7-052639 | 83.815740 | -5.444270 |
| 053528.1-051456 | 83.867420 | -5.249130 |
| 053528.1-051958 | 83.867327 | -5.333052 |

Table 4. COUP Source X-ray Photometry

| Source | | Extraction | | | | | Flux | | | Hardness | | | | | | |
|---|---|---|---|---|---|---|---|---|---|---|---|---|---|---|---|---|
| Seq # (1) | CXOONCJ (2) | Src Cts (3) | Bkg Cts (4) | Net Cts (5) | Area pix (6) | PSF Frac (7) | Exp ks (8) | Ct-Fl (a) (9) | IncFl (b) (10) | Med E keV (11) | HR1 (12) | ΔHR1 (13) | HR2 (14) | ΔHR2 (15) | HR3 (16) | ΔHR3 (17) |
| 1 | 053429.4-052337 | 883 | 89 | 793 | 664 | 0.50 | 500.4 | 0.283 | -4.897 | 1.28 | -0.59 | $^{+0.04}_{-0.04}$ | -0.54 | $^{+0.04}_{-0.03}$ | -0.34 | $^{+0.08}_{-0.08}$ |
| 2 | 053429.5-052354 | 1884 | 53 | 1830 | 1245 | 0.68 | 157.4 | 0.089 | -4.308 | 1.19 | -0.69 | $^{+0.02}_{-0.02}$ | -0.67 | $^{+0.02}_{-0.02}$ | -0.28 | $^{+0.05}_{-0.05}$ |
| 3 | 053433.9-052211 | 148 | 132 | 15 | 1541 | 0.89 | 382.0 | 0.216 | -6.737 | 0.88 | -1.00 | $^{+0.06}_{-\ldots}$ | -1.00 | $^{+0.40}_{-\ldots}$ | ... | ... |
| 4 | 053434.9-052507 | 327 | 310 | 16 | 1678 | 0.89 | 527.0 | 0.298 | -6.986 | 5.02 | 1.00 | $^{+\ldots}_{-0.00}$ | ... | ... | 1.00 | $^{+\ldots}_{-0.00}$ |
| 5 | 053438.2-052338 | 139 | 70 | 68 | 396 | 0.69 | 740.9 | 0.419 | -6.292 | 4.69 | 0.75 | $^{+0.19}_{-0.20}$ | -0.22 | $^{+0.45}_{-0.88}$ | 0.81 | $^{+0.17}_{-0.16}$ |
| 6 | 053438.2-052423 | 2260 | 372 | 1887 | 994 | 0.90 | 740.9 | 0.419 | -4.974 | 1.26 | -0.66 | $^{+0.04}_{-0.03}$ | -0.61 | $^{+0.03}_{-0.03}$ | -0.46 | $^{+0.11}_{-0.11}$ |
| 7 | 053439.7-052425 | 42315 | 362 | 41952 | 846 | 0.89 | 746.2 | 0.422 | -3.630 | 1.20 | -0.72 | $^{+0.00}_{-0.00}$ | -0.67 | $^{+0.00}_{-0.00}$ | -0.37 | $^{+0.01}_{-0.01}$ |
| 8 | 053439.8-052456 | 1349 | 219 | 1129 | 866 | 0.90 | 746.2 | 0.422 | -5.201 | 2.59 | 0.25 | $^{+0.04}_{-0.04}$ | 0.06 | $^{+0.05}_{-0.05}$ | 0.22 | $^{+0.04}_{-0.04}$ |
| 9 | 053439.9-052642 | 16471 | 199 | 16271 | 1318 | 0.99 | 385.5 | 0.218 | -3.757 | 1.34 | -0.59 | $^{+0.01}_{-0.01}$ | -0.57 | $^{+0.01}_{-0.01}$ | -0.27 | $^{+0.01}_{-0.01}$ |
| 10 | 053440.0-052604 | 388 | 235 | 152 | 1118 | 0.88 | 742.7 | 0.420 | -6.062 | 0.99 | -0.61 | $^{+0.25}_{-0.31}$ | -1.00 | $^{+0.23}_{-\ldots}$ | ... | ... |
| 11 | 053440.8-052242 | 5824 | 123 | 5700 | 691 | 0.88 | 693.2 | 0.392 | -4.415 | 1.53 | -0.40 | $^{+0.01}_{-0.01}$ | -0.39 | $^{+0.01}_{-0.01}$ | -0.18 | $^{+0.02}_{-0.02}$ |
| 12 | 053440.8-052639 | 374 | 42 | 331 | 228 | 0.39 | 702.0 | 0.397 | -5.297 | 1.79 | -0.15 | $^{+0.06}_{-0.06}$ | -0.27 | $^{+0.07}_{-0.07}$ | 0.03 | $^{+0.09}_{-0.09}$ |
| 13 | 053440.9-052559 | 325 | 250 | 74 | 970 | 0.89 | 746.2 | 0.422 | -6.380 | 1.11 | -1.00 | $^{+0.54}_{-\ldots}$ | -0.24 | $^{+0.24}_{-0.29}$ | -1.00 | $^{+0.89}_{-\ldots}$ |
| 14 | 053441.6-052357 | 349 | 136 | 212 | 666 | 0.89 | 721.5 | 0.408 | -5.908 | 1.00 | -0.82 | $^{+0.14}_{-0.14}$ | -0.80 | $^{+0.09}_{-0.08}$ | -0.69 | $^{+0.65}_{-\ldots}$ |
| 15 | 053441.7-052652 | 1758 | 282 | 1475 | 1103 | 0.88 | 698.5 | 0.395 | -5.034 | 1.29 | -0.45 | $^{+0.04}_{-0.04}$ | -0.62 | $^{+0.04}_{-0.03}$ | 0.13 | $^{+0.08}_{-0.08}$ |

[a]The units for the counts-to-flux conversion factor are $10^9$ ct cm$^2$ ph$^{-1}$.

[b]The units for the log Incident Flux are ph cm$^{-2}$ s$^{-1}$.

Note. — See §5 for descriptions of the columns. The full table of 1616 sources is provided in the electronic edition of the Journal.

Table 5. COUP Sources with Pileup Analysis

| Seq # | CXOONCJ | $r_{in}$ | $r_{out}$ | Net Counts | PSF Frac |
|---|---|---|---|---|---|
| | | $0.5''$pix | | | |
| 107 | 053455.9-052313 | 6.25 | 12.67 | 9004 | 0.08 |
| 123 | 053457.7-052351 | 5.00 | 11.95 | 5347 | 0.10 |
| 124 | 053457.7-052352 | 4.50 | 11.96 | 5074 | 0.13 |
| 245 | 053505.6-052519 | 3.50 | 11.73 | 2426 | 0.05 |
| 290 | 053507.4-052640 | 1.50 | 9.94 | 1895 | 0.51 |
| 394 | 053510.7-052344 | 2.50 | 9.14 | 4051 | 0.04 |
| 430 | 053511.5-052602 | 3.00 | 10.05 | 3621 | 0.06 |
| 450 | 053511.8-052149 | 4.00 | 9.95 | 5327 | 0.02 |
| 689 | 053515.2-052256 | 2.50 | 8.59 | 6931 | 0.03 |
| 724 | 053515.6-052256 | 4.00 | 8.54 | 3504 | 0.01 |
| 732 | 053515.7-052309 | 2.25 | 8.44 | 37523 | 0.04 |
| 745 | 053515.8-052314 | 2.25 | 8.39 | 21283 | 0.02 |
| 809[a] | 053516.4-052322 | 5.25 | 8.43 | 63444 | 0.01 |
| 854 | 053517.0-052232 | 2.25 | 8.64 | 3829 | 0.05 |
| 855 | 053517.0-052334 | 3.00 | 8.75 | 3364 | 0.02 |
| 881 | 053517.3-052544 | 3.75 | 9.73 | 4521 | 0.02 |
| 891 | 053517.5-051740 | 6.00 | 16.56 | 12686 | 0.17 |
| 932 | 053517.9-052245 | 4.50 | 8.45 | 6648 | 0.01 |
| 965 | 053518.3-052237 | 3.50 | 8.56 | 5939 | 0.02 |
| 1087 | 053520.1-052639 | 4.00 | 10.81 | 3792 | 0.02 |
| 1090 | 053520.2-052056 | 3.00 | 10.31 | 4306 | 0.05 |
| 1130 | 053521.0-052349 | 3.00 | 8.99 | 3843 | 0.03 |
| 1232 | 053522.8-052457 | 4.25 | 9.66 | 3525 | 0.01 |
| 1259 | 053523.6-052331 | 2.50 | 9.40 | 2183 | 0.04 |

[a]= $\theta^1$C Ori

Table 6. COUP Source X-ray Spectroscopy

| Seq # (1) | CXOONCJ (2) | $\log N_H$ $cm^{-2}$ (3) | $\Delta \log N_H$ $cm^{-2}$ (4) | $kT_1$ keV (5) | $\Delta kT_1$ keV (6) | $kT_2$ keV (7) | $\Delta kT_2$ keV (8) | $\log EM_1$ $cm^{-3}$ (9) | $\pm$ $cm^{-3}$ (10) | $\log EM_2$ $cm^{-3}$ (11) | $\pm$ $cm^{-3}$ (12) | $\chi^2_\nu$ (13) | dof Flag (14) | Fit Flag (15) | Model Flag (16) | Feature (17) |
|---|---|---|---|---|---|---|---|---|---|---|---|---|---|---|---|---|
| 1 | 053429.4-052337 | 20.67 | 0.43 | 0.85 | 0.12 | 4.37 | 0.95 | 52.17 | 0.11 | 52.62 | 0.04 | 1.15 | 33 | ··· | 20.1.2 | 000c0000 |
| 2 | 053429.5-052354 | 21.21 | 0.07 | 0.79 | 0.03 | 3.29 | 0.35 | 53.13 | 0.06 | 53.16 | 0.04 | 1.15 | 23 | ··· | 60.1.2 | 00000000 |
| 3 | 053433.9-052211 | 20.21 | 2.31 | 1.14 | 0.27 | ··· | ··· | 51.28 | 0.25 | ··· | | 0.70 | 24 | ··· | 05.1.1 | 00h00000 |
| 4 | 053434.9-052507 | 23.39 | 0.27 | 1.44 | 4.39 | ··· | ··· | 53.72 | 1.00 | ··· | | 0.65 | 58 | ··· | 05.1.1g | 0s000000 |
| 5 | 053438.2-052338 | 23.46 | 0.21 | 9.52 | 15.00 | ··· | ··· | 52.61 | 0.44 | ··· | | 1.15 | 24 | ··· | 05.1.1 | 0s000m00 |
| 6 | 053438.2-052423 | 21.12 | 0.12 | 0.78 | 0.09 | 2.32 | 0.27 | 52.16 | 0.12 | 52.68 | 0.04 | 1.15 | 28 | ··· | 60.1.2 | 000c0000 |
| 7 | 053439.7-052425 | 20.93 | 0.04 | 0.83 | 0.01 | 2.30 | 0.08 | 53.58 | 0.02 | 53.94 | 0.01 | 2.06 | 173 | m | 60.1.2 | l00000w0 |
| 8 | 053439.8-052456 | 22.05 | 0.05 | 15.00 | 8.48 | ··· | ··· | 52.81 | 0.02 | ··· | | 0.95 | 18 | ··· | 60.1.1 | 00000000 |
| 9 | 053439.9-052642 | 21.37 | 0.03 | 0.83 | 0.02 | 3.04 | 0.11 | 53.59 | 0.03 | 53.87 | 0.01 | 1.38 | 134 | p | 60.1.2g | 00000000 |
| 10 | 053440.0-052604 | 20.00 | 1.21 | 0.74 | 0.13 | ··· | ··· | 51.42 | 0.21 | ··· | | 0.77 | 44 | ··· | 07.1.1 | 00h00000 |
| 11 | 053440.8-052242 | 21.69 | 0.04 | 0.52 | 0.03 | 4.13 | 0.29 | 53.21 | 0.12 | 53.34 | 0.02 | 1.81 | 70 | p | 60.1.2 | l0000000 |
| 12 | 053440.8-052639 | 21.33 | 0.18 | 14.34 | 11.68 | ··· | ··· | 52.44 | 0.05 | ··· | | 0.68 | 32 | ··· | 10.1.1 | 00000000 |
| 13 | 053440.9-052559 | 20.00 | 2.12 | 12.58 | 15.00 | ··· | ··· | 51.51 | 0.17 | ··· | | 1.02 | 55 | ··· | 05.1.1 | 00h00p00 |
| 14 | 053441.6-052357 | 20.81 | 0.14 | 0.69 | 6.24 | 9.23 | 15.00 | 51.64 | 1.00 | 51.19 | 0.21 | 0.75 | 25 | ··· | 10.1.2 | 00hc0000 |
| 15 | 053441.7-052652 | 21.16 | 0.44 | 0.66 | 0.08 | 15.00 | 15.00 | 52.35 | 0.16 | 52.59 | 0.03 | 1.60 | 21 | m | 60.1.2 | 00h00000 |

Note. — See §7 for descriptions of the columns. The full table of 1616 sources is provided in the electronic edition of the Journal.

Table 7. COUP Source X-ray Variability

| Seq # (1) | CXOONCJ (2) | Gap Flag (3) | $\log P_{KS}$ (4) | BBNum (5) | BBMin ct ks$^{-1}$ (6) | ΔBBMin ct ks$^{-1}$ (7) | BBMax ct ks$^{-1}$ (8) | ΔBBMax ct ks$^{-1}$ (9) |
|---|---|---|---|---|---|---|---|---|
| 1 | 053429.4-052337 | ··· | -4.00 | 7 | 0.50 | 0.02 | 36.67 | 1.52 |
| 2 | 053429.5-052354 | ··· | -3.40 | 9 | 1.18 | 0.10 | 64.52 | 14.96 |
| 7 | 053433.9-052211 | ··· | -0.95 | 1 | 0.18 | 0.01 | 0.18 | 0.01 |
| 4 | 053434.9-052507 | ··· | -0.68 | 1 | 0.39 | 0.01 | 0.39 | 0.01 |
| 7 | 053438.2-052338 | ··· | -0.19 | 1 | 0.34 | 0.01 | 0.34 | 0.01 |
| 6 | 053438.2-052423 | ··· | -4.00 | 8 | 0.91 | 0.09 | 10.51 | 0.26 |
| 7 | 053439.7-052425 | ··· | -4.00 | 36 | 26.65 | 2.60 | 301.08 | 55.54 |
| 8 | 053439.8-052456 | ··· | -1.06 | 1 | 1.61 | 0.02 | 1.61 | 0.02 |
| 9 | 053439.9-052642 | ··· | -4.00 | 105 | 6.34 | 1.47 | 518.43 | 45.68 |
| 10 | 053440.0-052604 | ··· | -3.00 | 6 | 0.33 | 0.02 | 21.46 | 2.20 |
| 11 | 053440.8-052242 | ··· | -4.00 | 19 | 3.33 | 0.90 | 98.11 | 2.35 |
| 12 | 053440.8-052639 | ··· | -4.00 | 5 | 0.29 | 0.02 | 2.08 | 0.16 |
| 13 | 053440.9-052559 | ··· | -1.01 | 1 | 0.39 | 0.01 | 0.39 | 0.01 |
| 14 | 053441.6-052357 | ··· | -2.70 | 2 | 0.38 | 0.01 | 1.20 | 0.11 |
| 15 | 053441.7-052652 | ··· | -4.00 | 8 | 0.77 | 0.23 | 3.56 | 0.23 |

Note. — See §8 for descriptions of the columns. The full table of 1616 sources is provided in the electronic edition of the Journal.

Table 8. COUP Source X-ray Luminosities

| Seq # (1) | CXOONCJ (2) | $\log L_s$ erg $s^{-1}$ (3) | $\log L_h$ erg $s^{-1}$ (4) | $\log L_{h,c}$ erg $s^{-1}$ (5) | $\log L_t$ erg $s^{-1}$ (6) | $\log L_{t,c}$ erg $s^{-1}$ (7) |
|---|---|---|---|---|---|---|
| 1 | 053429.4-052337 | 29.51 | 29.50 | 29.50 | 29.81 | 29.84 |
| 2 | 053429.5-052354 | 30.11 | 29.95 | 29.96 | 30.34 | 30.47 |
| 3 | 053433.9-052211 | 28.12 | 27.42 | 27.42 | 28.20 | 28.22 |
| 4 | 053434.9-052507 | <27.00 | 29.09 | 30.04 | 29.09 | 30.65 |
| 5 | 053438.2-052338 | <27.00 | 29.05 | 29.62 | 29.05 | 29.80 |
| 6 | 053438.2-052423 | 29.47 | 29.31 | 29.32 | 29.69 | 29.79 |
| 7 | 053439.7-052425 | 30.82 | 30.57 | 30.57 | 31.01 | 31.08 |
| 8 | 053439.8-052456 | 28.86 | 29.81 | 29.85 | 29.85 | 30.01 |
| 9 | 053439.9-052642 | 30.64 | 30.62 | 30.64 | 30.93 | 31.08 |
| 10 | 053440.0-052604 | 28.37 | 27.11 | 27.11 | 28.39 | 28.39 |
| 11 | 053440.8-052242 | 29.92 | 30.17 | 30.20 | 30.36 | 30.63 |
| 12 | 053440.8-052639 | 28.95 | 29.47 | 29.48 | 29.58 | 29.64 |
| 13 | 053440.9-052559 | 28.22 | 28.54 | 28.54 | 28.71 | 28.71 |
| 14 | 053441.6-052357 | 28.60 | 28.25 | 28.25 | 28.76 | 28.82 |
| 15 | 053441.7-052652 | 29.35 | 29.58 | 29.59 | 29.78 | 29.86 |

Note. — See §9 for descriptions of the columns. The full table of 1616 sources is provided in the electronic edition of the Journal.

Table 9. Probable Optical Counterparts of COUP Sources

| Seq # (1) | CXOONCJ (2) | ID (3) | Off $''$ (4) | $V$ mag (5) | $I$ mag (6) | SpTy (7) | $A_V$ mag (8) | $\log T_{\rm eff}$ °K (9) | $\log L_{\rm bol}$ $L_\odot$ (10) | $R$ $R_\odot$ (11) | $M$ $M_\odot$ (12) | $\log t$ yr (13) | $\Delta(I-K)$ mag (14) | $EW$(Ca) Å (15) | $<V>$ mag (16) | $\Delta V$ mag (17) | $\pm$ mag (18) | $P$ day (19) |
|---|---|---|---|---|---|---|---|---|---|---|---|---|---|---|---|---|---|---|
| 1 | 053429.4-052337 | 8 | 0.39 | ··· | 15.73 | M5.5 | 0.00 | 3.483 | -0.98 | 1.18 | 0.14 | 6.16 | ··· | 0.0 | ··· | ··· | ··· | ··· |
| 2 | 053429.5-052354 | 5 | 4.85 | 12.01 | 10.97 | K1 | 0.29 | 3.708 | 0.64 | 2.69 | 1.98 | 6.58 | 0.01 | ··· | ··· | ··· | ··· | ··· |
| 3 | 053433.9-052211 | 25 | 6.43 | 17.76 | 15.22 | M4.5 | 0.00 | 3.500 | -0.88 | 1.21 | 0.17 | 5.95 | 0.52 | 0.0 | ··· | ··· | ··· | ··· |
| 4 | 053434.9-052507 | ··· | ··· | ··· | ··· | ··· | ··· | ··· | ··· | ··· | ··· | ··· | ··· | ··· | ··· | ··· | ··· | ··· |
| 5 | 053438.2-052338 | ··· | ··· | ··· | ··· | ··· | ··· | ··· | ··· | ··· | ··· | ··· | ··· | ··· | ··· | ··· | ··· | ··· |
| 6 | 053438.2-052423 | 40 | 0.36 | 17.37 | 14.48 | M3.5 | 0.46 | 3.518 | -0.57 | 1.60 | 0.27 | 6.31 | 0.12 | 0.0 | 14.40 | 0.06 | 0.16 | 9.81 |
| 7 | 053439.7-052425 | 45 | 0.75 | 11.38 | 09.89 | K1-K4 | 0.75 | 3.661 | 1.19 | 6.23 | 2.12 | 5.55 | -0.02 | ··· | ··· | ··· | ··· | ··· |
| 8 | 053439.8-052456 | ··· | ··· | ··· | ··· | ··· | ··· | ··· | ··· | ··· | ··· | ··· | ··· | ··· | ··· | ··· | ··· | ··· |
| 9 | 053439.9-052642 | 46 | 1.06 | 12.39 | 11.12 | K0-K3 | 0.88 | 3.708 | 0.73 | 2.96 | 2.11 | 6.49 | 0.10 | ··· | ··· | ··· | ··· | ··· |
| 10 | 053440.0-052604 | 48 | 1.02 | 20.10 | 15.50 | M6 | 1.71 | 3.471 | -0.37 | 2.49 | 0.18 | 5.15 | -0.69 | 1.0 | ··· | ··· | ··· | ··· |
| 11 | 053440.8-052242 | 50 | 0.70 | 13.40 | 11.65 | K1e-K7 | 0.42 | 3.602 | 0.44 | 3.46 | 0.69 | 5.74 | 1.37 | -14.6 | ··· | ··· | ··· | ··· |
| 12 | 053440.8-052639 | 51 | 1.36 | 16.82 | 14.45 | M1.5 | 0.77 | 3.555 | -0.57 | 1.35 | 0.39 | 6.45 | 1.05 | 0.0 | ··· | ··· | ··· | ··· |
| 13 | 053440.9-052559 | 53 | 1.14 | 18.65 | 15.85 | M0 | 2.58 | 3.580 | -0.71 | 1.02 | 0.55 | 6.93 | 1.13 | 1.5 | ··· | ··· | ··· | ··· |
| 14 | 053441.6-052357 | 54 | 0.76 | 18.85 | 15.27 | M5 | 0.77 | 3.494 | -0.68 | 1.57 | 0.20 | 6.34 | -0.04 | 0.0 | ··· | ··· | ··· | ··· |
| 15 | 053441.7-052652 | 55 | 0.94 | 17.07 | 14.40 | M3 | 0.31 | 3.526 | -0.60 | 1.48 | 0.29 | 6.33 | 0.36 | 1.0 | ··· | ··· | ··· | ··· |

Note. — See §10 for descriptions of the columns. The full table of 1616 sources is provided in the electronic edition of the Journal.

Table 10. Probable Near-Infrared Counterparts of COUP Sources

| COUP | | $JHK_s$ bands | | | | | | | | L band | | |
|---|---|---|---|---|---|---|---|---|---|---|---|---|
| Seq | CXOONCJ | Source | Off | $J$ | $H$ | $K_s$ | Src | Phot | Con | Ref | Src | $L$ |
| # | | | $''$ | mag | mag | mag | Flag | Flag | Flag | Flag | # | mag |
| (1) | (2) | (3) | (4) | (5) | (6) | (7) | (8) | (9) | (10) | (11) | (12) | (13) |
| 1 | 053429.4-052337 | 05342945-0523374 | 0.04 | 13.99 | 13.37 | 13.09 | ··· | AAA | ccc | ··· | ··· | ··· |
| 2 | 053429.5-052354 | 05342924-0523567 | 4.85 | 10.19 | 9.78 | 9.61 | ··· | AAA | 000 | ··· | ··· | ··· |
| 3 | 053433.9-052211 | 05343357-0522087 | 6.25 | 13.25 | 12.54 | 12.17 | ··· | AAA | 000 | ··· | ··· | ··· |
| 4 | 053434.9-052507 | ··· | ··· | ··· | ··· | ··· | ··· | ··· | ··· | ··· | ··· | ··· |
| 5 | 053438.2-052338 | ··· | ··· | ··· | ··· | ··· | ··· | ··· | ··· | ··· | ··· | ··· |
| 6 | 053438.2-052423 | 05343822-0524236 | 0.20 | 12.73 | 11.95 | 11.70 | ··· | AAA | 0d0 | ··· | ··· | ··· |
| 7 | 053439.7-052425 | 05343976-0524254 | 0.48 | 8.85 | 8.10 | 7.95 | ··· | AAA | 000 | ··· | ··· | ··· |
| 8 | 053439.8-052456 | ··· | ··· | ··· | ··· | ··· | ··· | ··· | ··· | ··· | ··· | ··· |
| 9 | 053439.9-052642 | 05343988-0526420 | 0.55 | 10.22 | 9.65 | 9.46 | ··· | AAA | 000 | ··· | ··· | ··· |
| 10 | 053440.0-052604 | 05344000-0526040 | 0.45 | 13.33 | 12.70 | 12.34 | ··· | AAA | 000 | ··· | ··· | ··· |
| 11 | 053440.8-052242 | 05344086-0522423 | 0.37 | 10.53 | 9.46 | 8.60 | ··· | AAA | 000 | ··· | ··· | ··· |
| 12 | 053440.8-052639 | 05344081-0526387 | 0.77 | 12.68 | 11.67 | 11.14 | ··· | AAA | 000 | ··· | ··· | ··· |
| 13 | 053440.9-052559 | 05344093-0526000 | 0.75 | 13.79 | 12.62 | 11.93 | ··· | AAA | 000 | ··· | ··· | ··· |
| 14 | 053441.6-052357 | 05344162-0523574 | 0.30 | 13.28 | 12.57 | 12.28 | ··· | AAA | 000 | ··· | ··· | ··· |
| 15 | 053441.7-052652 | 05344171-0526529 | 0.54 | 12.54 | 11.66 | 11.14 | ··· | AAA | 000 | ··· | ··· | ··· |

Note. — See §10 for descriptions of the columns. The full table of 1616 sources is provided in the electronic edition of the Journal.

Table 11. Upper Limits of Undetected Stars from Hillenbrand (1997)

| H97-Srs # (1) | R.A. (degrees J2000) (2) | Decl. (3) | LimCt cts (4) | Exp ks (5) | Conf Flag (6) | $V$ mag (7) | $I$ mag (8) | SpTy (9) | $A_V$ mag (10) | $\log T_{\rm eff}$ °K (11) | $\log L_{\rm bol}$ $L_\odot$ (12) | $R$ $R_\odot$ (13) | $M$ $M_\odot$ (14) | $\log t$ yr (15) | $\Delta(I-K)$ mag (16) | $EW$(Ca) Å (17) |
|---|---|---|---|---|---|---|---|---|---|---|---|---|---|---|---|---|
| 9 | 83.623192 | -5.395426 | 4017 | 396.2 | x | 18.94 | 14.74 | K5 | 8.21 | 3.695 | 1.06 | 4.63 | 1.61 | 5.43 | ··· | 2.9 |
| 23 | 83.639984 | -5.385887 | 67 | 715.2 | ··· | 13.08 | 12.00 | G7 | 0.82 | 3.740 | 0.38 | 1.71 | 1.50 | 6.83 | -0.10 | ··· |
| 42 | 83.661568 | -5.356926 | 53 | 720.7 | ··· | ··· | 16.41 | G: | ··· | ··· | ··· | ··· | ··· | ··· | ··· | 4.7 |
| 3060 | 83.674896 | -5.358895 | 44 | 688.1 | x | 18.60 | 16.27 | ··· | ··· | ··· | ··· | ··· | ··· | ··· | ··· | ··· |
| 3073 | 83.677109 | -5.379485 | 46 | 746.7 | ··· | ··· | 16.60 | ··· | ··· | ··· | ··· | ··· | ··· | ··· | ··· | ··· |
| 62 | 83.678688 | -5.421204 | 55 | 749.9 | ··· | 17.64 | 14.59 | early-K | 5.26 | 3.695 | 0.40 | 2.17 | 1.38 | 6.21 | -0.10 | 1.5 |
| 67 | 83.682404 | -5.424037 | 53 | 752.6 | ··· | ··· | 16.62 | ··· | ··· | ··· | ··· | ··· | ··· | ··· | ··· | ··· |
| 86 | 83.694984 | -5.434676 | 45 | 760.4 | ··· | 18.64 | 15.83 | ··· | ··· | ··· | ··· | ··· | ··· | ··· | ··· | ··· |
| 85 | 83.695068 | -5.358148 | 130 | 756.8 | x | 17.39 | 14.78 | M2.5 | 0.59 | 3.535 | -0.71 | 1.25 | 0.26 | 6.15 | 0.14 | 4.1 |
| 108 | 83.708405 | -5.312427 | 66 | 454.9 | x | 10.19 | 9.29 | A2-A7 | 2.07 | 3.940 | 2.01 | 4.46 | 3.59 | ··· | 0.63 | ··· |
| 141 | 83.729233 | -5.449654 | 208 | 667.4 | x | 18.27 | 15.43 | G: | ··· | ··· | ··· | ··· | ··· | ··· | ··· | 1.3 |
| 179 | 83.741188 | -5.478287 | 237 | 731.5 | x | ··· | 16.65 | M5.5 | 0.00 | 3.483 | -1.34 | 0.77 | 0.09 | 6.32 | ··· | 0.0 |
| 5084 | 83.754486 | -5.340973 | 24 | 789.3 | ··· | ··· | 16.99 | ··· | ··· | ··· | ··· | ··· | ··· | ··· | ··· | ··· |
| 214 | 83.757027 | -5.443426 | 23 | 702.6 | ··· | ··· | 16.75 | ··· | ··· | ··· | ··· | ··· | ··· | ··· | ··· | ··· |
| 219 | 83.758736 | -5.306343 | 35 | 765.1 | ··· | 19.82 | 15.52 | M5 | 2.62 | 3.494 | -0.33 | 2.35 | 0.15 | 4.43 | 0.12 | 0.3 |

Note. — The full table of 201 sources is provided in the electronic edition of the Journal.

Table 12. Upper Limits of Undetected Stars from the Two Micron All Sky Survey

| 2M-Src | LimCt cts | Exp ks | Conf Flag | $J$ mag | $H$ mag | $K_s$ mag | Phot Flag | Con Flag |
|---|---|---|---|---|---|---|---|---|
| (1) | (2) | (3) | (4) | (5) | (6) | (7) | (8) | (9) |
| 05342954-0523437 | 3891 | 383.9 | x | 11.90 | 10.70 | 10.11 | AAA | 000 |
| 05343297-0522142 | 475 | 126.4 | ··· | 16.63 | 15.30 | 14.60 | CUU | c00 |
| 05343359-0523099 | 66 | 715.2 | ··· | 11.28 | 10.78 | 10.72 | AAA | 000 |
| 05343419-0524593 | 615 | 490.2 | ··· | 18.65 | 16.20 | 15.13 | UCB | 000 |
| 05343508-0521498 | 1044 | 200.6 | ··· | 16.95 | 16.34 | 15.51 | UUC | 000 |
| 05343646-0521458 | 454 | 485.4 | ··· | 16.77 | 15.87 | 15.16 | BBB | 000 |
| 05343725-0525101 | 59 | 729.6 | ··· | 16.88 | 15.60 | 15.28 | CBB | 000 |
| 05343824-0524024 | 150 | 733.4 | ··· | 15.96 | 14.70 | 14.23 | AAA | 000 |
| 05343850-0523255 | 132 | 713.1 | x | 16.07 | 14.53 | 14.06 | AAA | 000 |
| 05343873-0521250 | 53 | 719.4 | ··· | 14.10 | 13.05 | 12.67 | AAA | 000 |
| 05344062-0523150 | 50 | 720.5 | ··· | 16.14 | 15.17 | 14.84 | AAA | 000 |
| 05344065-0526526 | 657 | 445.8 | x | 16.73 | 16.26 | 15.44 | BCB | ccc |
| 05344135-0524442 | 58 | 744.9 | ··· | 16.87 | 15.91 | 15.50 | CCB | ccc |
| 05344196-0521321 | 44 | 687.5 | ··· | 14.16 | 13.48 | 13.12 | AAA | 000 |
| 05344224-0522325 | 46 | 745.1 | ··· | 16.50 | 15.14 | 14.64 | BAA | c00 |

Note. — The full table of 1145 sources is provided in the electronic edition of the Journal. Note that some of these sources are bright spots in the diffuse nebular emission rather than stellar photospheres.